

Contents

Introduction	1
1 The Standard Model and Supersymmetry	2
1.1 The Standard Model	2
1.1.1 Electroweak Symmetry Breaking and the Higgs mechanism	6
1.1.2 Limitations of the Standard Model	9
1.2 Supersymmetry and the MSSM	11
1.2.1 Minimal Supersymmetric Standard Model	13
1.2.2 Phenomenology of Supersymmetry	16
2 The ATLAS Experiment at the LHC	20
2.1 The LHC	20
2.2 The ATLAS Detector	23
2.2.1 The Magnet System	24
2.2.2 The Inner Detector	25
2.2.3 The Calorimeters	28
2.2.4 The Muon Spectrometer	31
2.3 The ATLAS Trigger System	32
3 The ATLAS Trigger System	34
3.1 Overview	34
3.2 Level-1 Trigger	36
3.3 High-Level Trigger	39
3.3.1 Inner detector tracking	39
3.3.2 Performance of HLT	40
4 Event Simulation and Object Reconstruction	46
4.1 Generation of a MC-simulated event	46
4.2 Object Reconstruction	51
4.3 Object Selection	59
4.3.1 Baseline Object Selection	59
4.3.2 Overlap Removal	59

4.3.3	Signal Object Selection	59
5	Stop searches in final states with jets and missing transverse energy	60
6	Results and Statistical Intepretations	61
	Conclusion	62
	Appendix title	63
	List of Acronyms	64
	Bibliography	68

Introduction

Last thing to write

1 | The Standard Model and Supersymmetry

A theory is something nobody believes, except the person who made it. An experiment is something everybody believes, except the person who made it.

Albert Einstein

Section 1.1 presents an overview of the Standard Model ([SM](#)) of particle physics, together with its limitations (Section 1.1.2) and the need of an extension. One of the most popular of these extensions, Supersymmetry ([SUSY](#)), will be discussed in Section 1.2 where an overview of the theory and the motivations behind its success, will be presented. The description of the Minimal Supersymmetric Standard Model ([MSSM](#)) in Section 1.2.1, and finally the phenomenology of supersymmetry, with particular attention to third-generation supersymmetry (as the most relevant theoretical support to this work) will be discussed in Section 1.2.2.

1.1 The Standard Model

The [SM](#) is an effective theory that aims to provide a general description of fundamental particles and their interactions.

The 20th century can be considered a quantum revolution. Several experiments led to discoveries which were found to be, together with the formalised theory, a solid base of the [SM](#) of particle physics and our description of nature. Several particles were first predicted and then experimentally observed e.g. the W and the Z bosons, the τ lepton, [1], and more recently the Higgs boson at the Large Hadron Collider ([LHC](#)) discovered by the [ATLAS](#) [2] and [CMS](#) [3] collaborations.

The **SM** is a Quantum Field Theory (**QFT**) where particles are treated like excitations of quantum fields in a four-dimensional Minkowski space-time [4]. It can describe three of the four fundamental forces; weak, electromagnetic, and strong, but not gravity.

The most general classification of the elementary particles within the **SM** can be made by means of spin and their behaviour under Poincaré transformations [5]: *fermions* (leptons and quarks), usually referred to as matter particles, which have half-integer spin values, in unit of \hbar , and *bosons*, usually referred to as information carriers, which have integer-spin values. A noteworthy subset of bosons is formed by the Spin-1 bosons, also known as gauge bosons. These can be considered mediators of the forces. Figure 1.1 displays the elementary particles of the Standard Model known as of today.

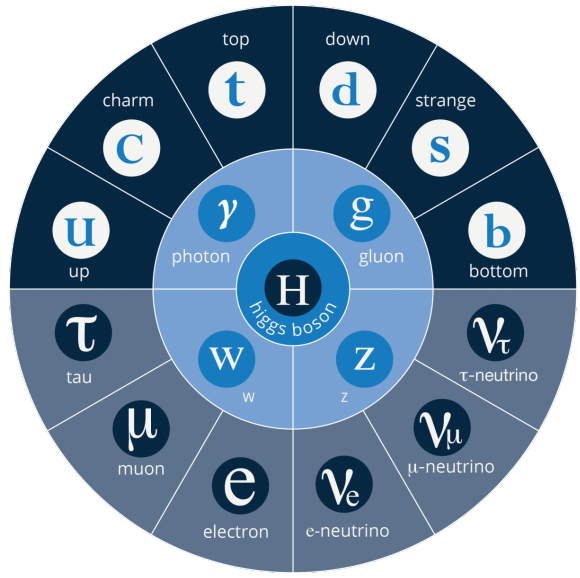


Figure 1.1: The elementary particles of the **SM**. From the outermost to the innermost; fermions (quarks, top-half wheel, leptons, bottom-half wheel), vector bosons, and the Higgs boson.

Symmetries and Gauge Groups

In 1915, the German mathematician and theoretical physicist Emmy Noether (23 March 1882 – 14 April 1935) proved that every differentiable symmetry of the action - defined as the integral over space of a Lagrangian density function $S = \int \mathcal{L} dt$ - of a physical system has a corresponding conservation law [6]. More generally, a symmetry is a property of a physical system and under certain transformations this property is preserved.

A gauge theory in **QFT**, is a theory in which the Lagrangian is invariant under a continuous group of local transformations. Group theory was adopted to describe the symmetries conserved in the **SM**. The gauge group of the **SM** is the *Lie Group* which contains all the transformations between possible gauges [5]. The Lie algebra of group generators is associated to any Lie group and for each group generator there emerges a corresponding field, called the gauge field, and the quanta of such fields are called *gauge bosons*.

The three **SM** interactions can therefore be mathematically described by the following;

$$U(1)_Y \otimes SU(2)_L \otimes SU(3)_C \quad (1.1)$$

Here, Y is the weak hypercharge, used to estimate the correlation between the electric charge (Q) and the third component of the weak isospin (I_3) via the relation $Q = I_3 + Y/2$, where I_3 can either be $\pm 1/2$ or 0 for left-handed and right-handed particles, respectively, and C the colour charge, L the left-handedness.

Quantum Electrodynamics (**QED**) is an Abelian gauge theory described by the symmetry group $U(1)$. The electromagnetic four-potential is its gauge field and the photon its gauge boson [7]. The interactions between charged fermions occurs by the exchange of a massless photon.

The weak interaction is described by the non-Abelian gauge group $SU(2)$. The $SU(2)$ generators are the massless gauge bosons $W_\mu^{\alpha=1,\dots,3}$ and they violate the parity by acting only on left-handed particles. As a consequence of non-Abelianity, $SU(2)$ gauge bosons can self-interact as the generator commutators are non-vanishing. Additionally, quarks can also interact through weak interaction as mixtures of **SM** eigenstates as described by the CKM matrix [8].

Finally, the strong interaction, described by the symmetry group $SU(3)$, has eight massless gauge bosons, the gluons, $G_\mu^{\alpha=1,\dots,8}$ which can be exchanged between quarks and can also self-interact.

Fermions

There are twelve fermions in the **SM**: six quarks and six leptons. In particular, fermions can be grouped into three generations. Each generation contains four particles; one up- and one down-type quark, one charged lepton and one neutral lepton. The masses of the charged leptons and quarks increase with the generation. The six quarks of the **SM** can be grouped into three $S(2)$ doublets;

$$\begin{pmatrix} u \\ d \end{pmatrix}, \quad \begin{pmatrix} c \\ s \end{pmatrix}, \quad \begin{pmatrix} t \\ b \end{pmatrix}$$

The up-type quarks (*up, charm, top*) have charge $+\frac{2}{3}e$ and the down-type quarks (*down, strange, beauty/bottom*) have charge $-\frac{1}{3}e$, where e is the electron charge. Quarks also have another quantum number that can be seen as the analogue of the electric charge; the colour charge. This can exist in three different states; *red, green* and *blue*, but they cannot

exist as free particles. They rather group to form hadronic matter, also known as *hadrons*. There are two kinds of hadrons; mesons and baryons. Mesons are quark-antiquark systems, e.g. the pion, and baryons are three-quark system, e.g. protons and neutrons. Quarks and anti-quarks have a baryon number of $\frac{1}{3}$ and $-\frac{1}{3}$, respectively.

There are six leptons and they can be classified in charged leptons (electron e , muon μ , tau τ) and neutral leptons (electron neutrino ν_e , muon neutrino ν_μ , tau neutrino ν_τ).

$$\begin{pmatrix} \nu_e \\ e^- \end{pmatrix}, \quad \begin{pmatrix} \nu_\mu \\ \mu^- \end{pmatrix}, \quad \begin{pmatrix} \nu_\tau \\ \tau^- \end{pmatrix}$$

Each lepton has a characteristic quantum number, called lepton number (L). Negatively (positively) charged leptons have $L = -1$ ($L = 1$) and neutral leptons have $L = 1$. The lepton number is conserved in all the interactions.

Forces of Nature

Forces in the [SM](#) are described by gauge theories, where the interactions are mediated by a vector gauge boson.

[QED](#) describes the electromagnetic force, which only affects charged leptons (neutrinos are instead affected by the weak force, mediated by the W^\pm and Z^0 bosons) and quarks and it is mediated by the photon (γ).

The weak interaction is associated with handedness (the projection of a particle spin onto its direction of motion). Both leptons and quarks have left- and right-handed components. However, only the left-handed (right-handed) component for neutrinos (anti-neutrinos) has been observed. This means that nature prefers to produce left-handed neutrinos and right-handed anti-neutrinos, which is the so-called *parity violation* [9].

The strong interaction, mediated by the gluon, electrically neutral and massless, is described by Quantum Chromodynamics ([QCD](#)). Its coupling (α_s) increases with increasing distance and is smaller at short range. In particular, α_s evolves as a function of the transferred four-momentum squared, Q^2 , as follows:

$$\alpha_s(Q^2) \propto \frac{1}{n_f \log\left(\frac{Q^2}{\Lambda_{\text{QCD}}^2}\right)} \tag{1.2}$$

where n_f is the number of quarks with mass below Q^2 and Λ_{QCD} is the [QCD](#) characteristic scale. Eq. 1.2 shows that α_s decreases as a function of Λ_{QCD} , but at the same time it

quickly diverges when Q^2 gets closer to Λ . In other words, as the condition $\alpha_s \ll 1$ only holds for $Q^2 \gg \Lambda_{\text{QCD}}$, QCD can be treated perturbatively¹ only at high energy scales². Furthermore, QCD has three important features:

- *confinement*: quarks or gluons cannot be observed as free particles, but only colourless “singlet” states can be observed as “jets”, namely collimated cone-shaped sprays of hadrons;
- *asymptotic freedom*: interactions between quarks and gluons become weaker as the energy scale increases and the corresponding length scale decreases, as $\alpha_s \rightarrow 0$ for $Q^2 \rightarrow \infty$
- *hadronisation*: when quarks or gluons are pulled apart, the production of pairs of hadrons, produced from the vacuum, is energetically preferred to an increase in distance.

Table 1.1 summarises the forces described in the SM and the main characteristics of the mediators. The gravitational force is believed to be mediated by the graviton, but as already mentioned, since it is not included in the SM, it will not be further discussed.

Table 1.1: Forces and mediators described by the SM

Force	Name	Symbol	Mass [GeV]	Charge
Electromagnetic	Photon	γ	0	0
Weak	W	W^\pm	80.398	$\pm e$
	Z	Z^0	91.188	0
Strong	Gluon	g	0	0

1.1.1 Electroweak Symmetry Breaking and the Higgs mechanism

In 1979 Sheldon Glashow, Abdus Salam, and Steven Weinberg were awarded the Nobel Prize in Physics for their contributions to the so-called electroweak unification [10, 11, 12]. In the mathematical description of the SM in 1.1, the electroweak interaction is described by $U(1)_Y \otimes SU(2)_L$.

The four electroweak physical bosons W^\pm , Z and γ are related to the four unphysical gauge bosons $W_\mu^{\alpha=1,\dots,3}$ and B_μ . In particular, to obtain the physical bosons the gauge

¹ Perturbation theory (quantum mechanics) is an approximation to describe a complicated quantum system in terms of a simpler one.

² Perturbation theory can only be used when the coupling constant (expansion parameter) is small.

bosons have to mix as follows;

$$A_\mu = W_\mu^3 \sin \theta_W + B_\mu \cos \theta_W \quad (1.3)$$

$$Z_\mu = W_\mu^3 \cos \theta_W - B_\mu \sin \theta_W \quad (1.4)$$

$$W_\mu^\pm = \frac{1}{\sqrt{2}} (W_\mu^1 \mp i W_\mu^2) \quad (1.5)$$

Here, θ_W is the so-called *Weinberg angle* which is the angle by which spontaneous symmetry breaking rotates the original gauge bosons W_μ^3 and B_μ into the physical Z and γ . A_μ and Z_μ are the photon and the Z boson fields, respectively. The θ_W angle can be experimentally determined in terms of the coupling strengths, of the $B_\mu(g_1)$ and the $W_\mu^\alpha(g_2)$ to the fermions, using the relation $\tan \theta_W = g_1/g_2$.

The mass terms for both gauge bosons and fermionic fields are forbidden by the electroweak gauge as they are not invariant under gauge transformations. Nonetheless, it was experimentally proven that W and Z bosons are massive [7], therefore in order for the **SM** assumption to hold, the electroweak symmetry must be broken.

The **SM** Lagrangian can be written as the sum of the various Lagrangians describing the three interactions and the masses of the elementary particles as follows:

$$\mathcal{L}_{\text{SM}} = \mathcal{L}_{\text{EWK}} + \mathcal{L}_{\text{QCD}} + \mathcal{L}_{\text{Mass}} \quad (1.6)$$

In order for the **SM** Lagrangian to remain a re-normalisable theory, the mass terms ($\mathcal{L}_{\text{Mass}}$) cannot be inserted by hand. A mechanism, that can preserve the gauge symmetry in the **SM** and can solve the inconsistency arisen from the mass difference between the gauge bosons and the physical ones is needed. A British theoretical physicist, Peter Higgs (29 May 1929, Newcastle upon Tyne, UK), came up with a brilliant solution for which he was awarded the Nobel Prize in Physics in 2013. Higgs proposed [13] that broken symmetry in the electroweak theory could explain the origin of masses of elementary particles, and in particular of W and Z bosons. The mechanism introduces a scalar field, known as the Higgs field, thought to couple to both massive fermions and bosons. The $SU(2)$ doublet is then introduced in the **SM**;

$$\phi = \begin{pmatrix} \phi^+ \\ \phi^0 \end{pmatrix} \quad (1.7)$$

with ϕ^+ and ϕ^0 generic complex fields:

$$\phi^+ = \frac{\phi_1 + i\phi_2}{\sqrt{2}}, \quad \phi^0 = \frac{\phi_3 + i\phi_4}{\sqrt{2}} \quad (1.8)$$

Consider a Lagrangian of the form:

$$\mathcal{L}_{\text{Higgs}} = (\partial_\mu \phi)^* (\partial^\mu \phi) - V(\phi) \quad (1.9)$$

Re-normalisability and $SU(2)_L \otimes U(1)_Y$ invariance require the Higgs potential to be of the following form:

$$V(\phi) = \mu^2 \phi^\dagger \phi + \lambda \left(\phi^\dagger \phi \right)^2 \quad (1.10)$$

The Lagrangian in Eq. 1.9 is the Higgs Lagrangian if ϕ is chosen to be the following:

$$\phi = \begin{pmatrix} \phi^+ \\ \phi^0 \end{pmatrix} = \begin{pmatrix} G^+ \\ \frac{1}{\sqrt{2}}(v + H + iG^0) \end{pmatrix}$$

Here, the complex scalar field G^\pm and the real scalar field G^0 correspond to Goldstone bosons, and the real scalar field H is the **SM** Higgs boson field [14]. These massless scalars are absorbed due to the gauge transformations by the electroweak gauge bosons of the **SM**:

$$\phi = \begin{pmatrix} \phi^+ \\ \phi^0 \end{pmatrix} = \begin{pmatrix} 0 \\ \frac{1}{\sqrt{2}}(v + H) \end{pmatrix} \quad (1.11)$$

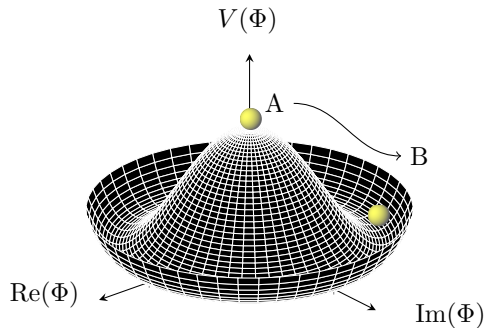


Figure 1.2: The Higgs potential in the complex plane.

The Higgs potential in Eq. 1.10 is displayed in Fig. 1.2 if λ and μ are chosen to be real. Such potential has a non-zero ground state, v , also known as Vacuum Expectation Value (VEV):

$$\phi_0 = \begin{pmatrix} 0 \\ \frac{1}{\sqrt{2}}v \end{pmatrix} \quad (1.12)$$

Such representation remains invariant under $U(1)$ allowing electric charge conservation. However, the SM gauge symmetry 1.1 is broken into $SU(2)_L \otimes U(1)_Y$.

In summary, to generate particle masses gauge symmetry must be broken. However, in order for the theory to remain re-normalisable, the global Lagrangian symmetry must be preserved. This can be solved introducing the concept of *spontaneous* symmetry breaking (SSB): a mechanism that allows a symmetric Lagrangian, but not a symmetric vacuum. In particular, given a Lagrangian invariant under a certain transformation, T_X , and a generic set of states, that transform under T_X as the elements of a multiplet, the symmetry is spontaneously broken if one of those states is arbitrarily chosen as the ground state of the system. The interaction of the Higgs field with the $SU(2) \otimes U(1)$ gauge fields, $W_\mu^{\alpha=1,2,3}$, result in the three gauge bosons fields acquiring mass whilst the A_μ field remains massless.

1.1.2 Limitations of the Standard Model

The SM has been extensively validated at the Large Electron-Positron Collider (LEP) (European Organization for Nuclear Research (CERN)) first. Run 1 of the LHC extended the validation beyond the energy limits of LEP (200 GeV) as shown in Fig. 1.3: the agreement, between the measured production cross-section of various SM processes and the SM predictions, looks very good. However, there are some fundamental questions that still have no answer.

Hierarchy Problem

Due to the coupling of the Higgs field to the fermionic fields, the one-loop corrections to the Higgs mass receive several contributions [16]. In particular, looking at Fig. 1.4:

$$\Delta m_H^2 = -\frac{|\lambda_f|^2}{8\pi^2} \Lambda_{\text{UV}}^2 + \dots \quad (1.13)$$

where, λ_f is the coupling constant to the fermionic field; Δm_H^2 is the difference between the observed Higgs mass m_H^2 and the bare mass, m_H^0 (Lagrangian parameter); Λ_{UV} is the

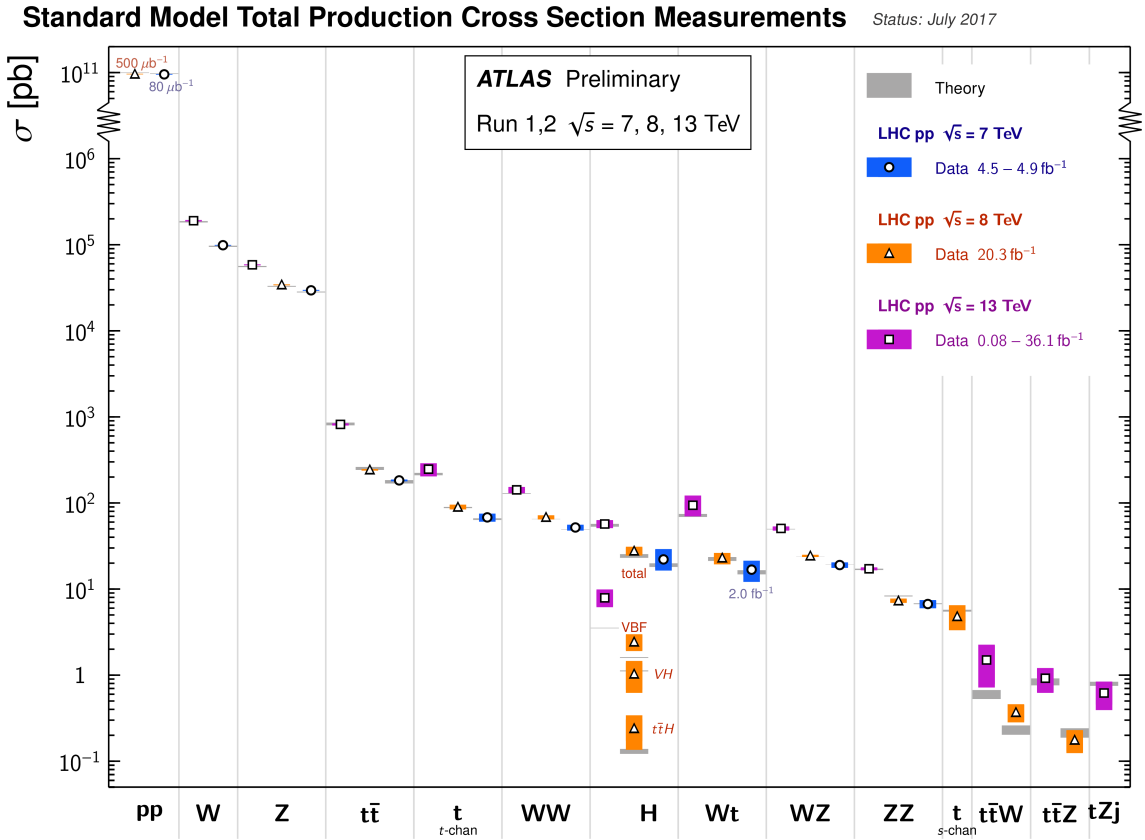


Figure 1.3: Summary of several SM total production cross-section measurements, corrected for leptonic branching fractions, compared to the corresponding theoretical expectations. All theoretical expectations were calculated at NLO or higher. The luminosity used for each measurement is indicated close to the data point. Uncertainties for the theoretical predictions are quoted from the original ATLAS papers. They were not always evaluated using the same prescriptions for PDFs and scales. Not all measurements are statistically significant yet [15].

ultraviolet momentum cut-off, selected to be at the Planck scale ($\sim 2 \cdot 10^{18}$ GeV), at which a QFT description of gravity is believed to become possible. The correction to the Higgs mass will be around 30 orders of magnitude larger than Higgs mass itself, in opposition to what has been measured. This difference just mentioned, between the electroweak scale and the Planck scale arisen from the quantum corrections to the Higgs mass, is the so-called Hierarchy Problem [16].

Neutrino Masses

The Super-Kamiokande Collaboration in 1998 [17], and SNO Collaboration in 2001 [18], have provided measurements of the neutrino flux from solar and atmospheric sources. The Nobel Prize in Physics 2015 was awarded jointly to Takaaki Kajita and Arthur B. McDonald “for the discovery of neutrino oscillations, which shows that neutrinos have mass” [19]. Such feature contradicts the description of the neutrinos in the SM, which are assumed to be massless, therefore there needs to be a mechanism that generates neutrino

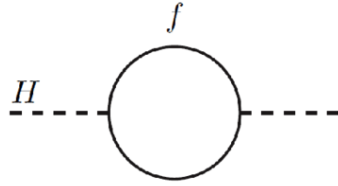


Figure 1.4: One-loop quantum corrections to the Higgs mass. A fermion correction with coupling λ_f .

masses. One possibility would be to add Majorana mass terms or adding additional right-handed neutrinos with a very heavy mass, known as the see-saw mechanism [20].

Dark Matter

Although Dark Matter (DM) has never been directly observed, its existence is inferred from its gravitational effects. For example, looking at galaxies rotation, it was observed that the rotation speed was higher than expected, given the amount of visible matter [21]. Two different reasoning arose during the last century to justify such effect: there is either matter that cannot be seen by us (in terms of visible light), which contributes to the galactic mass, or the general relativity works differently at galactic distances. The former is believed to be the most likely and it implies the existence of new particles which do not interact via electromagnetic interaction, the so-called Weakly Interacting Massive Particle (WIMP) [22].

1.2 Supersymmetry and the MSSM

One of the main motivations for SUSY is the cancellation of quadratic divergences to Δm_H^2 via the introduction of the so-called SUSY particles with a half-integer spin difference with respect to their SM partners. This provides a solution to the hierarchy problem as the Higgs mass squared potential receives corrections from a new scalar of mass of the form:

$$\Delta m_H^2 = -\frac{|\lambda_S|^2}{16\pi^2} \left[\Lambda_{\text{UV}}^2 - 2m_S^2 \ln(\Lambda_{\text{UV}}/m_S) + \dots \right] \quad (1.14)$$

where, λ_S is the coupling of SUSY particles to the Higgs field. This term cancels the fermionic contributions in Eq. 1.13 since the couplings are the same, which means that the experimentally measured mass of the Higgs boson can be obtained without performing any unnatural *tuning* of the parameters [23, 24]. This is what makes SUSY a *natural theory*³.

³ The Naturalness of a theory is a property for which dimensionless ratios between free parameters should

The running of gauge coupling constants⁴ is predicted by the **SM**, but, as previously mentioned, although the electroweak unification occurs at ~ 100 GeV, it is not the case for the strong force. In the **MSSM**, a supersymmetric extension of the **SM**, due to addition of *new* particles involved in the gauge interactions, a new set of coefficients arise. As shown in Fig. 1.5 the three lines, representing electromagnetic (dashed blue), weak (dashed red) and strong (solid green) interactions respectively, do not meet at one point, but they do with the introduction of supersymmetry. This can therefore be considered an approximate unification, of all three gauge couplings, at the Planck scale, which is an indication for a potential Grand Unification Theory (**GUT**) that could be obtained within a supersymmetric model. In addition, together with the unification at the **GUT** scale, another good motivation for **SUSY** searches is that, if **SUSY** is **MSSM**-like (m_{SUSY} not heavier than ~ 1 TeV), it can be discovered at the **LHC**.

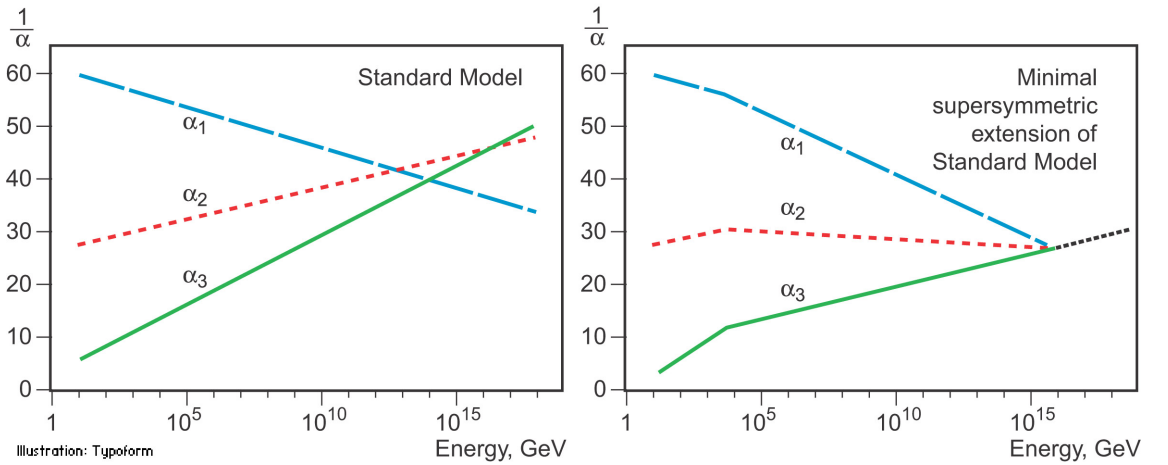


Figure 1.5: The inverse couplings of electromagnetic (dashed blue), weak (dashed red) and strong (solid green) interactions with the **SM** (left) and a supersymmetric model (right). In the **SM** the three lines do not meet at one point, but with the introduction of supersymmetry, and assuming that the supersymmetric particles are not heavier than about 1 TeV, they do meet.

SUSY introduces a space-time symmetry that relates bosons to fermions and vice-versa, via a transformation of the form of:

$$Q |\text{fermion}\rangle = |\text{boson}\rangle, \quad Q |\text{boson}\rangle = |\text{fermion}\rangle \quad (1.15)$$

For each **SM** particle there exists a supersymmetric partner, generally called *sparticle* (where the s stands for “scalar”), with a spin difference of $\Delta s = 1/2$. Each pair of partners is arranged in a so-called *supermultiplet*. The two components have same masses and quantum numbers, but different spin, due to their relation to the Q operator (and its properties).

⁴ assume sensible values and that free parameters are not fine-tuned.

⁴ The coupling strength, as a function of energy, is calculable given a value at a fixed scale.

Sleptons and *squarks* interact as their **SM** equivalent, namely for example, the superpartners of the left-handed paragraph* fermion components couple weakly, while the superpartners of the right-handed **SM** fermion components do not. Gauge supermultiplets contain a vector boson and two spin- $\frac{1}{2}$ fermions. Spin-1 bosons are arranged in gauge multiplets, and their superpartners, referred to as *gauginos*, are spin- $\frac{1}{2}$ fermions. Unlike the **SM**, the Spin-0 Higgs boson has two supermultiplets containing sparticles with different weak isospin values, referred to as H_u and H_d , which are required to give mass to both the up- and down-type sparticles. Higgs **SUSY** partners are called the *Higgsinos*.

As of today, **SUSY** particles have not been observed, resulting in the assumption that **SUSY** must be a broken symmetry, otherwise superpartners would have the same masses as their **SM** equivalent. However, if sparticles were to be too heavy (close to the Planck scale), the hierarchy problem would be re-introduced and therefore would still remain unsolved. The *soft SUSY* breaking mechanism, described in Section 1.2.1, overcomes this problem by imposing constraints on the masses of sparticles to a range that can be experimentally explored.

1.2.1 Minimal Supersymmetric Standard Model

There does not exist a unique extension of a supersymmetric **SM**, i. e. **SUSY** is not a well-defined model but it is more a framework within which various **SM** extensions can be derived. The **MSSM**, a minimal supersymmetric extension of the **SM** [25], is defined by essentially doubling up the number of particles in the **SM** theory in order to include all the **SM** particles as well as their corresponding superpartners.

Soft SUSY breaking

The mass spectrum of the **SUSY** particles must sit somewhere at a larger scale than the **SM** one, as supersymmetric particles have not been discovered at the mass scale of their **SM** partners. This gives us a hint that supersymmetry cannot be an exact symmetry and therefore it is broken. There has to be an analogy with the electroweak symmetry breaking discussed in 1.1.1, where the symmetry is broken by a non-zero **VEV**. The mechanism must be spontaneous in order for the broken supersymmetry to still provide a solution to the hierarchy problem: a big alteration of the relationship between the fermionic and scalar couplings will result in a non-cancellation of the corrections to the Higgs mass squared parameter. This equates to adding terms to the **SUSY** Lagrangian which are gauge invariant and violate **SUSY**, but contain only masses and couplings with positive

mass dimension. The total Lagrangian is defined as;

$$\mathcal{L}_{\text{MSSM}} = \mathcal{L}_{\text{SUSY}} + \mathcal{L}_{\text{soft}} \quad (1.16)$$

where all the additional terms are contained within $\mathcal{L}_{\text{soft}}$ and the original **SUSY** invariant interaction terms are contained within $\mathcal{L}_{\text{SUSY}}$. A new set of parameters is then introduced into this **SM** extension. These parameters determine the mixing between the flavour eigenstates and the **SUSY** phenomenology, which will be discussed in Section 1.2.2.

MSSM mass spectrum

As per the **SM** gauge bosons, the gaugino masses are affected by electroweak symmetry breaking. The new states, introduced in the $\mathcal{L}_{\text{soft}}$, mix to form the mass eigenstates of the sparticles. The neutral Winos, \tilde{W}^0 , Binos, \tilde{B}^0 and Higgsinos \tilde{H}^0 mix to form the four *neutralinos* $\tilde{\chi}_i^0$ ($i = 1, 2, 3, 4$) as follows;

$$\begin{pmatrix} \tilde{\chi}_1^0 \\ \tilde{\chi}_2^0 \\ \tilde{\chi}_3^0 \\ \tilde{\chi}_4^0 \end{pmatrix} = \begin{pmatrix} M_1 & 0 & -c_\beta s_W m_Z & c_W s_\beta m_Z \\ 0 & M_2 & c_\beta c_W m_Z & -c_W s_\beta m_Z \\ -c_\beta s_W m_Z & c_\beta s_W m_Z & 0 & -\mu \\ s_\beta c_W m_Z & -s_\beta c_W m_Z & -\mu & 0 \end{pmatrix} \begin{pmatrix} \tilde{B}^0 \\ \tilde{W}^0 \\ \tilde{H}_u^0 \\ \tilde{H}_d^0 \end{pmatrix} \quad (1.17)$$

Here, $c_\beta = \cos \beta$, $(s_\beta) = \sin \beta$, $c_W = \cos \theta_W$ and $(s_W) = \sin \theta_W$. M_1 , M_2 are related to gaugino masses and μ to Higgsinos mass, $\tan \beta$ is the ratio of the **VEVs** of the two Higgs doublet fields, θ_W is the ratio of the electroweak coupling constants and, m_Z (m_W) is the mass of the Z (W) boson. The neutralino indices are conventionally assumed to increase with their masses. The charged winos \tilde{W}^\pm and Higgsinos \tilde{H}^\pm mix to form four *charginos*, $\tilde{\chi}_i^\pm$ ($i = 1, 2$) as it follows;

$$\begin{pmatrix} \tilde{\chi}_1^\pm \\ \tilde{\chi}_2^\pm \end{pmatrix} = \begin{pmatrix} M_2 & \sqrt{2}m_W s_\beta \\ \sqrt{2}m_W c_\beta & \mu \end{pmatrix} \begin{pmatrix} \tilde{W}^\pm \\ \tilde{H}^\pm \end{pmatrix} \quad (1.18)$$

Charginos and neutralinos mix as described in Eq. 1.18 and 1.17 and will be referred to as bino-like, wino-like or higgsino-like depending on their phenomenology. Gluinos do not mix as they carry colour charge.

The Higgs sector is also affected. There are five mass eigenstates, h^0 , H^0 , A^0 , and H^\pm . These, together with the other **MSSM** particles are listed in Table 1.2.

Table 1.2: SUSY particles in the MSSM

Name	Spin	Gauge Eigenstates	Mass Eigenstates
Squarks (\tilde{q})	0	$\tilde{u}_L \tilde{u}_R \tilde{d}_L \tilde{d}_R$	(same)
		$\tilde{c}_L \tilde{c}_R \tilde{s}_L \tilde{s}_R$	(same)
		$\tilde{t}_L \tilde{t}_R \tilde{b}_L \tilde{b}_R$	$\tilde{t}_1 \tilde{t}_2 \tilde{b}_1 \tilde{b}_2$
Sleptons (\tilde{l})	0	$\tilde{e}_L \tilde{e}_R \tilde{\nu}_L$	(same)
		$\tilde{\mu}_L \tilde{\mu}_R \tilde{\nu}_L$	(same)
		$\tilde{\tau}_L \tilde{\tau}_R \tilde{\nu}_\tau$	$\tilde{\tau}_1 \tilde{\tau}_2 \tilde{\nu}_\tau$
Higgs bosons	0	$H_u^0 H_d^0 H_u^+ H_d^-$	$h^0 H^0 A^0 H^\pm$
Neutralinos ($\tilde{\chi}_j^0$)	1/2	$\tilde{B}^0 \tilde{W}^0 \tilde{H}_u^0 \tilde{H}_d^0$	$\tilde{\chi}_1^0 \tilde{\chi}_2^0 \tilde{\chi}_3^0 \tilde{\chi}_4^0$
Charginos ($\tilde{\chi}_i^\pm$)	1/2	$\tilde{W}^\pm \tilde{H}_u^+ \tilde{H}_u^-$	$\tilde{\chi}_1^\pm \tilde{\chi}_2^\pm$
Gluino	1/2	\tilde{g}	(same)
Gravitino	3/2	\tilde{G}	(same)

In the **MSSM** the squark sector is specified by the mass matrix in the basis $(\tilde{q}_L, \tilde{q}_R)$ with $\tilde{q} = \tilde{t}$ or \tilde{b} [26]. A rotation matrix can be defined also for left- and right-handed squarks and sleptons, although in the **MSSM** the mixing is assumed to be non-zero only for the third-generation scalar partners. Stop, \tilde{t}_L, \tilde{t}_R , sbottom \tilde{b}_L, \tilde{b}_R , and stau, $\tilde{\tau}_L, \tilde{\tau}_R$ rotate into mass eigenstates, $\tilde{t}_1, \tilde{t}_2, \tilde{b}_1, \tilde{b}_2, \tilde{\tau}_1, \tilde{\tau}_2$, respectively, as described in Eq. 1.19 [27].

$$\mathcal{M}_{\tilde{q}}^2 = \begin{pmatrix} m_{\tilde{q}_L}^2 & a_q m_q \\ a_q m_q & m_{\tilde{q}_R}^2 \end{pmatrix} \quad (1.19)$$

with

$$\begin{aligned} m_{\tilde{q}_L}^2 &= M_Q^2 + m_Z^2 \cos 2\beta \left(I_3^{q_L} - e_q \sin^2 \theta_W \right) + m_q^2, \\ m_{\tilde{q}_R}^2 &= M_{\{\tilde{U}, \tilde{D}\}}^2 + m_Z^2 \cos 2\beta e_q \sin^2 \theta_W + m_q^2, \\ a_q m_q &= \begin{cases} (A_t - \mu \cot \beta) m_t, & (\tilde{q} = \tilde{t}) \\ (A_b - \mu \tan \beta) m_t, & (\tilde{q} = \tilde{b}) \end{cases} \end{aligned} \quad (1.20)$$

Here, $I_3^{q_L}$ is the third component of the weak isospin and e_q the electric charge of the quark q . $M_{\{\tilde{Q}, \tilde{U}, \tilde{D}\}}$ and $A_{t,b}$ are soft **SUSY**-breaking parameters, μ is the higgsino mass parameter, and $\tan \beta$, as previously mentioned, is the ratio of Higgs field **VEVs**. By diagonalising the matrix in Eq. 1.19 one gets the mass eigenstates

$$\tilde{q}_1 = \tilde{q}_L \cos \theta_{\tilde{q}} + \tilde{q}_R \sin \theta_{\tilde{q}} \quad (1.21)$$

$$\tilde{q}_2 = -\tilde{q}_L \sin \theta_{\tilde{q}} + \tilde{q}_R \cos \theta_{\tilde{q}} \quad (1.22)$$

with the mass eigenvalues $m_{\tilde{q}_1}, m_{\tilde{q}_2}$ ($m_{\tilde{q}_1} < m_{\tilde{q}_2}$) and the mixing angle $\theta_{\tilde{q}}$ ($-\pi/2 < \theta_{\tilde{q}} \leq \pi/2$).

1.2.2 Phenomenology of Supersymmetry

As previously mentioned, the introduction of **SUSY** particles overcomes the problem of an unnatural fine-tuning to the Higgs mass due to its quadratic corrections.

R-parity

The most general **MSSM** can contain operators that violate baryon and/or lepton number, thus allowing proton decays. The non-observation of proton decays forbids the existence of such terms. A possibility to avoid these operators is to introduce a new discrete symmetry named *R*-parity. The conserved quantum number is defined as;

$$P_R = (-1)^{3(B-L)+2s} \quad (1.23)$$

where B , L , and s are the baryon, lepton, and spin number, respectively.

The **SM** particles have $R = 1$ and **SUSY** partners have $R = -1$. When *R*-parity conservation is imposed on **MSSM** models, the mixing between particles and sparticles cannot occur, resulting in the number of **SUSY** particles to be even at every interaction vertex. Furthermore, all sparticles must be pair-produced and the Lightest Supersymmetric Particle (**LSP**) has to be stable and can be a good Dark Matter candidate.

Although **SUSY** searches in an *R*-parity violating (RPV) scenario have been extensively investigated by the particle-physics community, in this work only *R*-parity conserving (RPC) models, where the $\tilde{\chi}_1^0$ is assumed to be the **LSP**, were considered.

Phenomenological **MSSM** (pMSSM)

As mentioned in 1.2.1, once the **SUSY** soft breaking occurred, the unconstrained **MSSM** has more than 100 parameters in addition to the **SM** ones. This makes the **SUSY** searches, e. g. finding regions, in parameter space, that are consistent with the data, rather impractical. However, the number of free parameters can be reduced down to 19 if the following assumptions are made;

- no new source of CP-violation (CKM matrix is the only source)
- no Flavour Changing Neutral Currents ([FCNC](#))
- masses of the first- and second-generation sfermions are identical (first- and second-generation universality)

The introduction of such parameters, summarised in Table 1.3, defines the so-called Phenomenological [MSSM](#) ([pMSSM](#)).

Table 1.3: Parameters in the pMSSM.

Parameter	Description	N. of parameters
M_1, M_2, M_3	Bino, Wino and gluino masses	3
M_A	pseudo-scalar Higgs boson mass	1
μ	higgsino mass	1
$m_{\tilde{q}}, m_{\tilde{u}_R}, m_{\tilde{d}_R}$,	first- and second-generation squark masses	3
$m_{\tilde{Q}_L}, m_{\tilde{t}}, m_{\tilde{b}}$	third generation squark masses	3
$m_{\tilde{l}}, m_{\tilde{e}_R}$	first- and second-generation slepton masses	2
$m_{\tilde{L}}, m_{\tilde{\tau}_R}$	third-generation slepton masses	2
A_t, A_b, A_τ	third-generation trilinear couplings	3
$\tan \beta$	two-higgs-doublet fields VEVs ratio	1

Such parameter space is still rather large and it makes [pMSSM](#) searches extremely challenging and difficult to exclude. To overcome this problem *simplified models* are introduced. In other words, a certain signal process is extracted from the model and only particles contributing to a certain decay mode will be considered, e.g. $\tilde{t}_1 \rightarrow t + \tilde{\chi}_1^0$ only targets the 2-body decay ignoring the remaining [SUSY](#) mass spectrum. The number of parameters will then boil down to 2; $m_{\tilde{t}}$ and $m_{\tilde{\chi}^0}$, allowing the reinterpretation of the results and providing a powerful tool to constrain various models.

In this work only analyses based on such simplified models will be presented.

Phenomenology of the top squark

Fig. 1.6 shows [SUSY](#) particles production cross-sections in pp collisions at $\sqrt{s} = 13$ TeV for squarks that do not contribute to gluino production diagrams and vice versa, i.e. treating squarks and gluinos as *decoupled* making the cross-section of squark pair-production be the same for all families. While gluino pair-production cross-sections are fairly large, [SUSY](#) electroweak production cross-sections of neutralinos and charginos are considerably lower. Slepton production cross-section, which is not displayed, would sit just below higgsino-like chargino/neutralino production cross-section.

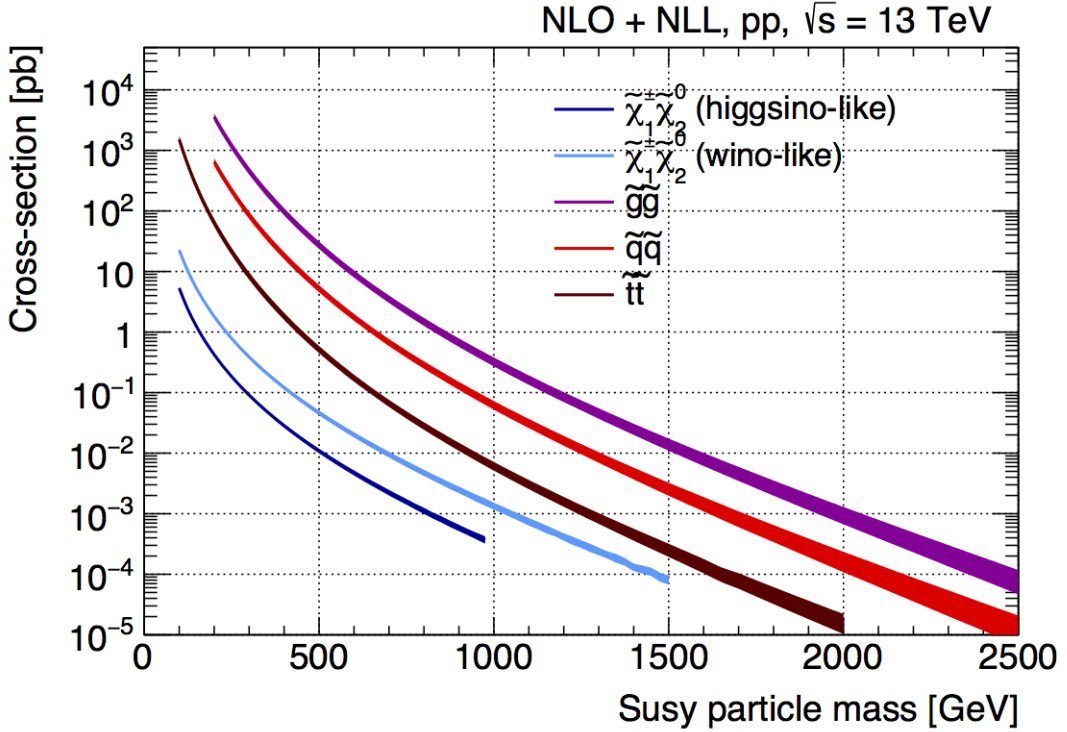


Figure 1.6: NLO+NLL production cross-sections as a function of mass at $\sqrt{s} = 13 \text{ TeV}$ [28]

There exists various decay modes of pair-produced stops, depending on the masses of the decay products;

- $\tilde{t} \rightarrow t \tilde{\chi}_1^0$
- $\tilde{t} \rightarrow b \tilde{\chi}_1^\pm \rightarrow b W \tilde{\chi}_1^0$ (on/off-shell W) or $\tilde{t} \rightarrow b W \tilde{\chi}_1^0$ (off-shell top)
- $\tilde{t} \rightarrow c \tilde{\chi}_1^0$
- $\tilde{t} \rightarrow b f f' \tilde{\chi}_1^0$

Figure 1.7 shows a schematic representation of the parameter space $(m_{\tilde{t}_1}, m_{\tilde{\chi}_1^0})$ and the different region where each of the above-mentioned process dominates.

In the models considered in this work, either $\tilde{\chi}_2^0$ or $\tilde{\chi}_1^\pm$ is assumed to be the so-called Next Lightest Supersymmetric Particle (NLSP). Three different decay scenarios were considered in this work; (a) where both top squarks decay via $\tilde{t} \rightarrow t^{(*)} \tilde{\chi}_1^0$ ⁵; (b) at least one of the stops decays via $\tilde{t} \rightarrow b \tilde{\chi}_1^\pm \rightarrow b W^{(*)} \tilde{\chi}_1^0$; (c) where $m_{\tilde{\chi}_1^0}$ is small enough to allow one stop to decay via $\tilde{t} \rightarrow t \tilde{\chi}_2^0 \rightarrow h/Z \tilde{\chi}_1^0$. Here, h is the SM Higgs boson (125 GeV), as illustrated in Figure 1.8(a)–(c), respectively. Furthermore, top squarks can also be indirectly produced through the so-called gluino-mediated stop production, as shown in Figure 1.8(d).

⁵ The symbol (*) indicates the off-shell production

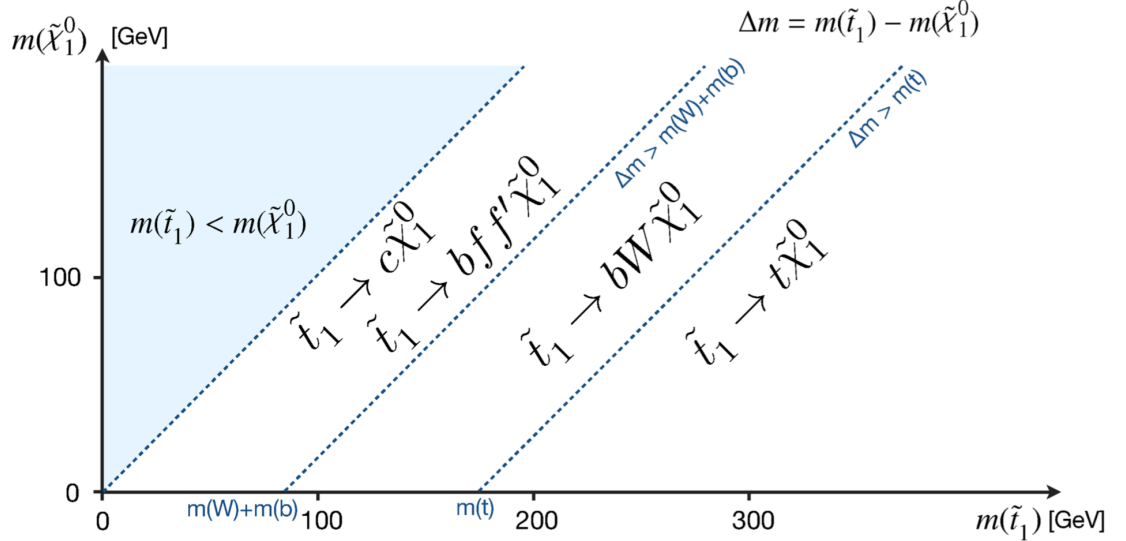


Figure 1.7: Illustration of stop decay modes in the $(m_{\tilde{t}_1}, m_{\tilde{\chi}_1^0})$ mass place where the $\tilde{\chi}_1^0$ is assumed to be the lightest supersymmetric particle. The dashed blue lines indicate thresholds separating regions where different processes dominate.

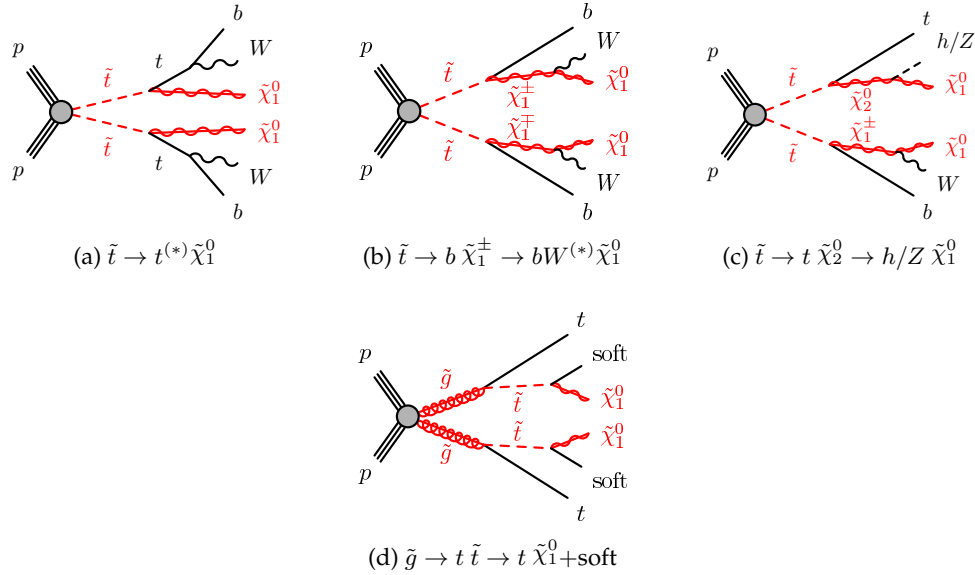


Figure 1.8: Diagrams of the decay topologies of the signal models considered in this work. The term “soft” refers to decay products that have transverse momenta below the detector thresholds.

Third-generation SUSY analyses, e. g. stop pair-production ($t\bar{t}$) or sbottom pair-production ($b\bar{b}$) are very challenging, due to the cross-section being around a factor of six smaller than $t\bar{t}$ production (when $m_{\tilde{t}_1} \sim m_t$), which usually is one of the main backgrounds. Furthermore, the cross-section of such processes dramatically decreases with increasing $m_{\tilde{q}}$. Nonetheless, for example, searches for direct \tilde{t}_1 production with $\tilde{t}_1 \rightarrow t + \tilde{\chi}_1^0$ are sensitive in a scenario where $m_{\tilde{t}_1} \gg m_t + m_{\tilde{\chi}_1^0}$ as the large E_T^{miss} , from the neutralinos, provides discriminating power for $t\bar{t}$ rejection.

2 | The ATLAS Experiment at the LHC

We are rather like children, who must take a watch to pieces to see how it works.

Sir Ernest Rutherford

A Toroidal LHC ApparatuS ([ATLAS](#)) is one of the four main experiments¹ taking data at a centre-of-mass energy of 13 TeV using beams delivered by the [LHC](#). In this chapter an overview of the [LHC](#) will be given in Section 2.1, then the [ATLAS](#) detector will be described in Section 2.2, and finally the Trigger system, used to cleverly select the data, will be described in Section 2.3. A more in-depth description of the Trigger algorithms I have been involved in will be given in Chapter 3.

2.1 The LHC

As of today, the [LHC](#) [29] is the world's largest and most powerful particle accelerator. It was designed to help answer some of the fundamental open questions in particle physics by colliding protons at an unprecedented energy and luminosity. It is located at [CERN](#), in the Geneva area, at a depth ranging from 50 to 175 metres underground. It consists of a 27-kilometre ring made of superconducting magnets, and inside it two high-energy particle beams travel in opposite directions and in separate beam pipes.

The beams are guided around the ring by a strong magnetic field generated by coils - made of special electric cables - that can operate in a superconducting regime. A total of 1232 superconducting dipole and 392 quadrupole magnets, with an average magnetic field of 8.3 T, are employed and kept at a temperature below 1.7 K, in order to preserve

¹ [ATLAS](#), Compact Muon Solenoid ([CMS](#)), A Large Ion Collider Experiment ([ALICE](#)), Large Hadron Collider Beauty ([LHCb](#))

their superconducting properties. The former are used to bend the beams and the latter to keep them focused while they get accelerated.

The collider first went live on September 2008 even though, due to a magnet quench incident that damaged over 50 superconducting magnets, it has been operational since November 2009 when low-energy beams circulated in the tunnel for the first time since the incident. This also marked the start of the main research programme and the beginning of the so-called Run 1: first operational run (2009 - 2013).

Performance of the LHC

In June 2015 the [LHC](#) restarted delivering physics data, after a two-year upgrade programme, the so-called Long Shut down 1 ([LS1](#)), during which the magnets were upgraded to handle the current required to circulate 7-TeV beams. It was the beginning of the so-called Run 2 - second operational run (2015-2018) - during which the [LHC](#) has collided up to 10^{11} bunches of protons every 25 ns at the design luminosity² of $2 \cdot 10^{34} \text{ cm}^{-2} \text{s}^{-1}$. The definition of the luminosity is:

$$\mathcal{L} = f \frac{n_b N_1 N_2}{4\pi\sigma_x\sigma_y} \quad (2.1)$$

where N_1 and N_2 are the number of protons per bunch in each of the colliding beams, f is the revolution frequency of the bunch collisions, n_b the number of proton per bunch, and σ_x and σ_y are the horizontal and vertical dimensions of the beam. The luminosity is strictly related to the number of collisions occurring during a certain experiment via the following:

$$\mathcal{N}_{\text{event}} = \mathcal{L}\sigma_{\text{event}} \quad (2.2)$$

where σ_{event} is the cross section of the process under investigation. It has not only collided protons but also heavy ions, in particular lead nuclei at $\sqrt{s_{NN}} = 5.02 \text{ TeV}$, at a luminosity of $10^{27} \text{ cm}^{-2} \text{s}^{-1}$ [30].

Acceleration stages

Before reaching the maximum energy, the proton beams are accelerated by smaller accelerators through various stages. Figure 2.1 shows a sketch of the [CERN](#)'s accelerator

² the highest luminosity the detector was designed to cope with

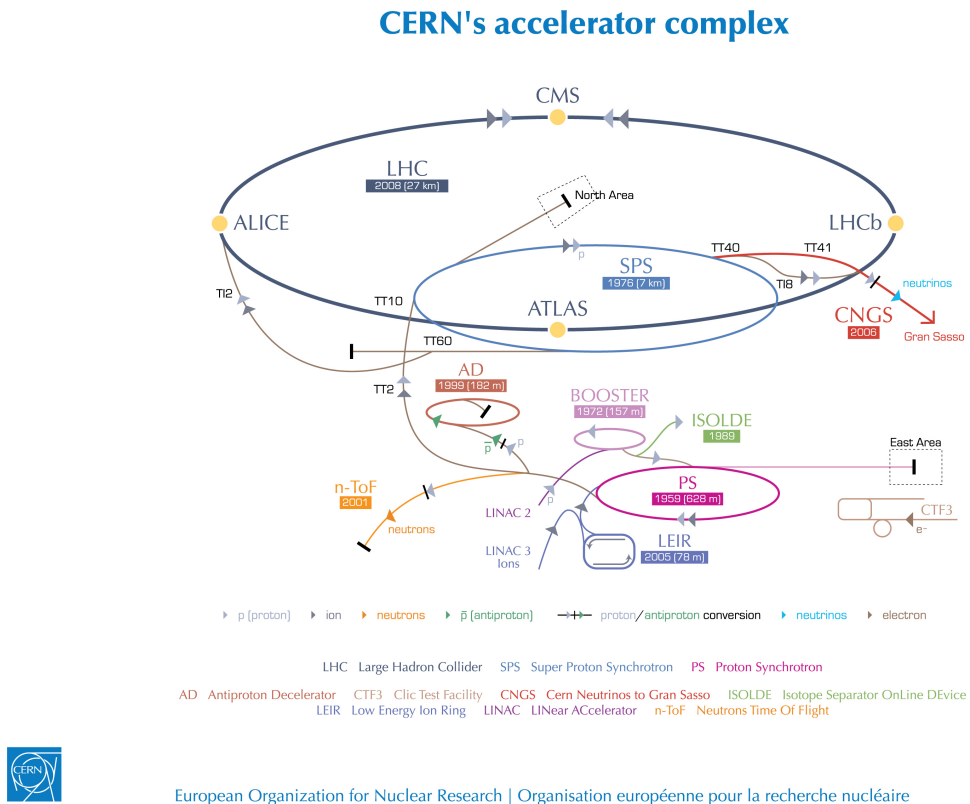


Figure 2.1: CERN Accelerator complex. The LHC is the last ring (dark grey line). Smaller machines are used for early-stage acceleration and also to provide beams for other experiments [31].

complex. It all begins with the Linear Accelerator 2 (LINAC2). Here protons are accelerated up to 50 MeV, and then injected in the Proton Synchrotron Booster (PSB) where they reach 1.4 GeV. The next stage is the Proton Synchrotron (PS), which boosts the beams up to 25 GeV and then Super Proton Synchrotron (SPS) makes them reach energies up to 450 GeV. Eventually, the beams are injected in bunches with a 25 ns spacing into the LHC, where they travel in opposite directions, while they are accelerated to up to a centre-of-mass energy of 13 TeV. Once the bunches reach the maximum energy, they are made collide at four different points, inside four experiments around the ring [29].

The heavy ion beams acceleration procedure is slightly different. Their journey starts at Linear Accelerator 3 (LINAC3), and the Low Energy Ion Ring (LEIR) then, before they make their way into the PS where they follow the same path as the protons.

The four large detectors on the collision points are; the multi-purpose detectors ATLAS [32], and CMS [33], LHCb [34], which focuses on flavour physics, and ALICE [35] which specialises in heavy ion physics. The *big four* are not the only experiments at the CERN's accelerator complex. There also are smaller experiments based at the the four caverns about the collision points e.g. TOTal cross section, Elastic scattering and diffraction dissociation Measurement at the LHC (TOTEM) [36], Large Hadron Collider forward (LHCf) [37] and Monopole & Exotics Detector At the LHC (MoEDAL) [38], but these will not be discussed

any further.

2.2 The ATLAS Detector

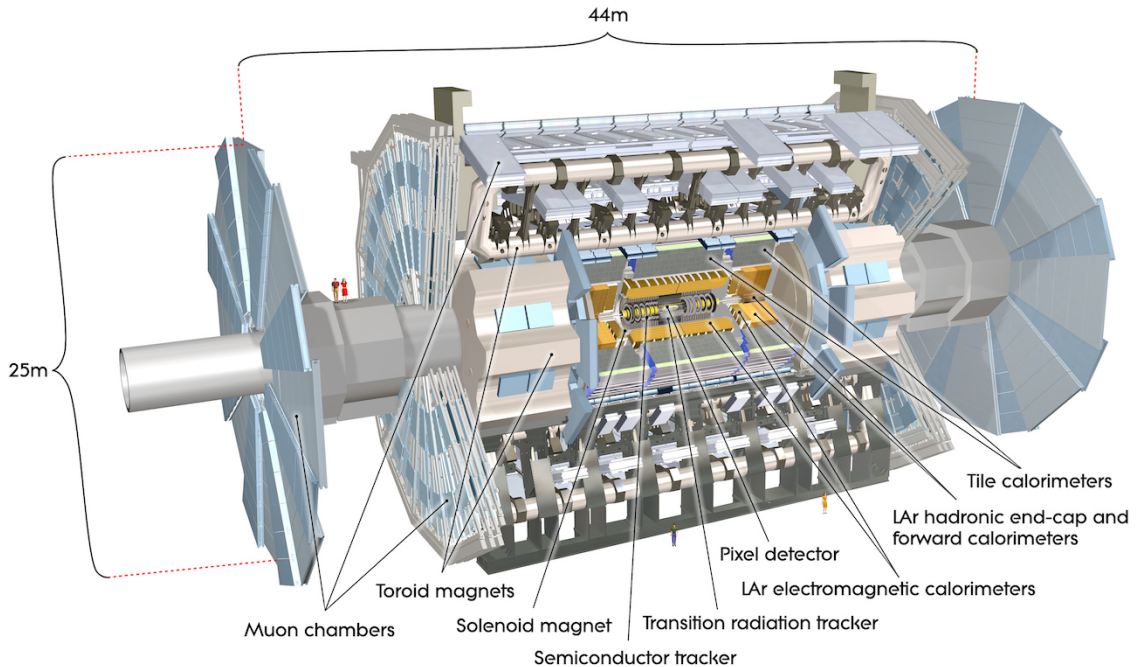


Figure 2.2: Cut-away view of the [ATLAS](#) detector. The dimensions of the detector are 25 m in height and 44 m in length. The overall weight of the detector is approximately 7000 tonnes [31].

[ATLAS](#) is a general-purpose detector designed to collect data with the highest luminosity provided by the [LHC](#). It is located at [CERN](#)'s Point 1 cavern and it measures about 45 m in length and 25 m in diameter. It has a forward-backward symmetric cylindrical geometry with respect to the interaction point and it is designed to reconstruct and measure physics objects such as electrons, muons, photons and hadronic jets. Its design was optimised to be as sensitive as possible to the discovery of the Higgs boson and Beyond Standard Model ([BSM](#)) physics. In fact, thanks to its various sub-systems, [ATLAS](#) is able to observe all possible decay products by covering nearly 4π steradians of solid angle.

In Figure 2.2 a cut-away view of [ATLAS](#) with all its components is shown. The innermost layer is the Inner Detector ([ID](#)) which is the core of the tracking system and consists of a Pixel, a SemiConductor Tracker ([SCT](#)), and a Transition Radiation Tracker ([TRT](#)). It is submerged in a 2 T magnetic field, generated by a thin superconducting solenoid, which bends all the charged particles' trajectories allowing transverse momentum measurement. The electromagnetic and hadronic calorimeters form the next layer and they are both used to perform precise energy measurements of photons, electrons, and hadronic jets. Finally, the outermost layer corresponds to the Muon Spectrometer ([MS](#)), enclosed

in a toroidal magnetic field, which, together with the ID, allows precise measurement of momentum and position of muons. These sub-detectors will be discussed in more detail in the following sections.

The ATLAS coordinate system

A coordinate system is taken on for the spatial definition of the sub-systems and kinematic measurement of physics processes. Such system is defined starting from the interaction point, defined as the origin. The z -axis is defined by the beam direction and the $x - y$ plane, as transverse to the beam direction.

A quantity, known as pseudo-rapidity, (η), is defined to describe the angle of a particle coming out of the collision, with respect to the beam axis:

$$\eta \equiv -\ln(\tan(\theta/2))$$

Here θ is the polar angle. The azimuthal angle, ϕ , is defined around the beam axis and the polar angle. In the (η, ϕ) space a distance ΔR can be therefore defined as

$$\Delta R = \sqrt{\Delta\eta^2 + \Delta\phi^2}$$

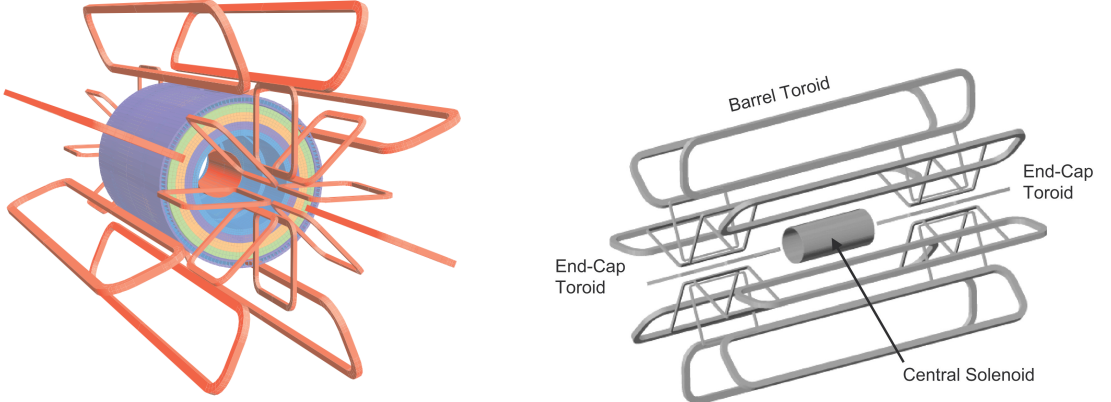
where $\Delta\eta$ and $\Delta\phi$ are the differences in pseudo-rapidity and azimuthal angle between any two considered objects. A central and a forward region of pseudo-rapidity are also defined such that the detector components are described as part of the *barrel* if they belong to the former or as part of the *end-caps* if they belong to the latter.

2.2.1 The Magnet System

The ATLAS magnet system, 26 m long with a 22 m diameter, generates the magnetic field needed to bend the trajectories of charged particles in order to perform momentum measurement. Figure 2.3a and 2.3b show the geometry of the system and its components, which are made of NbTi - superconducting material - and will be described in the following paragraphs.

The Central Solenoid

With an axial length of 5.8 m, an inner radius of 2.46 m, and an outer radius of 2.56 m, the central solenoid magnet is located between the ID and the Electromagnetic Calori-



(a) Geometry of magnet windings and tile calorimeter steel. The eight barrel toroid coils, with the end-cap coils interleaved are visible. The solenoid winding lies inside the calorimeter volume [32].

(b) Schematic view of the superconducting magnets [39].

Figure 2.3: The [ATLAS](#) magnet system.

meter ([ECAL](#)). Its function is to bend the charged particles that go through the [ID](#) and it is aligned on the beam axis providing a 2 T axial magnetic field that allows accurate momentum measurement up to 100 GeV [39].

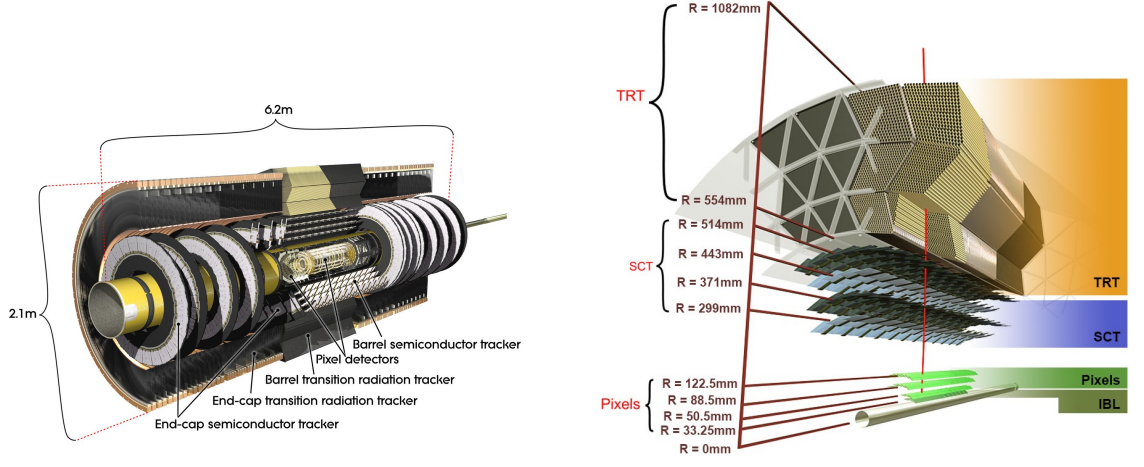
The Barrel and the End-cap Toroids

Figure 2.3b displays the toroid magnetic system that surrounds the calorimeters. With its cylindrical shape this component consists of a barrel and two end-caps toroids. The barrel toroid is comprised of eight coils and produces an approximately 0.5 T toroidal magnetic field for the central muon detectors. The end-cap toroids, also comprised of eight coils each, produce an approximately 1 T toroidal magnetic field, which is required to provide bending power for the end-cap regions of the muon spectrometer.

2.2.2 The Inner Detector

The [ID](#) [40] is the innermost component of the [ATLAS](#) detector i.e. the nearest sub-detector to the interaction region and it is used to reconstruct charged particle tracks used in the selection of physics objects. In fact, it allows robust track reconstruction, with accurate impact parameter resolution ($\sim 20\mu m$) and precise primary and Secondary Vertex ([SV](#)) reconstruction for charged particles (tracks) above 500 MeV and within $|\eta| < 2.5$.

The [ID](#) is comprised of independent and concentric sub-systems, which are all shown in Figure 2.4:



(a) Overview of the [ATLAS ID](#) with labels and dimensions.

(b) Diagram of the [ATLAS ID](#) and its sub-detectors.

Figure 2.4: The [ATLAS](#) Inner Detector

- [Insertable B-Layer \(IBL\)](#):

innermost Pixel Detector layer added during [ATLAS](#) Run 2 upgrade (2013/2014) to improve vertexing, by a factor ~ 1.4 , and impact parameter reconstruction, by a factor 2;

- [Silicon Pixel Tracker \(Pixel\)](#):

made of silicon pixel layers and used mainly for reconstructing both the primary and secondary vertices in an event;

- [SCT](#):

comprised of silicon micro-strip layers; thanks to its resolution ($17 \times 580 \mu\text{m}$) it can accurately measure particle momenta;

- [TRT](#):

final layer comprised of various layers of gaseous straw tube elements surrounded by transition radiation material.

These sub-detectors will be discussed in the following sections.

IBL

The [IBL](#) [41] is the innermost Pixel Detector layer as shown in Figure 2.4b. It is comprised of 6M channels and each pixel measures $50 \times 250 \mu\text{m}$. Its resolution is $8 \times 40 \mu\text{m}$. The addition of this new layer produced an improvement on the quality of the impact parameter reconstruction of tracks almost by a factor 2, and almost by a factor 1.4 on the

resolution of the reconstructed Primary Vertex ([PV](#)), highly important e. g. for the tagging of bottom-quark-initiated jets (*b*-jets).

Pixel

The Pixel detector is comprised of 1750 identical sensorchip-hybrid modules, each covering an active area of 16.4×60.8 mm. The total number of modules correspond to roughly 80 million semiconductor silicon pixels. The nominal pixel size is $50 \mu\text{m}$ in the ϕ direction and $400 \mu\text{m}$ in the barrel region, along the z -axis (beam axis) [42]. The reason why such a large amount of pixels is employed is justified by the need to cope with the high luminosity in [ATLAS](#). The silicon pixel detector measures 48.4 cm in diameter and 6.2 m in length providing a pseudo-rapidity coverage of $|\eta| < 2.5$. Figure 2.4b shows the three concentric barrel layers placed at 50.5 mm, 88.5 mm and 122.5 mm respectively. Furthermore, the Pixel detector is made of six disk layers, three for each forward region, such that when a charged particle crosses the layers it will generate a signal at least in three space points. The fine granularity of such detector allows accurate measurement and precise vertex reconstruction, as it provides a more accurate position measurement as a large detection area is available. In particular, it has a resolution of $10 \times 115 \mu\text{m}$.

SCT

The [SCT](#) is made of 4088 modules of silicon micro-strip detectors arranged in four concentric barrel layers. It is mainly used for precise momentum reconstruction over a range $|\eta| < 2.5$ and it was designed for precision measurement of the position using four points (corresponding to eight silicon layers), obtained as track hits when crossing the layers. Figure 2.4b shows the structure of the [SCT](#) with its four concentric barrel layers with radii ranging from 299 mm to 514 mm and two end-cap layers. Each module has an intrinsic resolution of $17 \mu\text{m}$ in the $R - \phi$ direction and $580 \mu\text{m}$ in the z direction. As the [SCT](#) is further away from the beam-pipe than the Pixel detector, it has to cope with reduced particle density. This allows for reduced granularity maintaining the same level of performance of the Pixel detector: [SCT](#) can use ~ 6.3 million read-out channels.

TRT

The last and outermost of the sub-systems in the [ID](#) is the [TRT](#). It is a gaseous detector which consists of 4 mm diameter straw tubes wound from a multilayer film reinforced with carbon fibres and containing a $30 \mu\text{m}$ gold plated tungsten wire in the centre. The straw is filled with a gas mixture of 70% Xe, 27% CO₂ and 3% O₂ [43]. As shown in Figure 2.4b, its section consists of three concentric layers with radii ranging from 554 mm to

1082 mm, each of which has 32 modules containing approximately 50,000 straws, 1.44 m in length, aligned parallel to the beam direction with independent read-out at both ends. The gas is ionised when a charged particle passes through it and electrons (ions) are collected at the anode (cathode). A current in the wire will be created and as the electric field in the tube is known, the distance from the wire can be calculated using the time that electrons take to drift to the wire. Furthermore, the **TRT** is capable of performing particle identification on the particles that pass through it by utilising the detection of transition radiation photons that are emitted when a highly relativistic charged particle crosses a boundary between two media with different dielectric constants. The separation between, e.g. electrons and charged pions is achieved by observing the amount of transition radiation produced, since this is dependent on how relativistic the charged particle is.

The **TRT** has an intrinsic resolution of $130 \mu\text{m}$ and, on average, 35 hits are observed within such sub-system when a charged particle passes through.

Performance of the ID

As previously mentioned, the tracking performed by the **ID** is indispensable to measure the properties of objects such as leptons and jets, as well as interaction vertices in a certain event and secondary vertices, which are used e.g. to identify bottom-quark-initiated jets(b -jets). Both jets and b -jets are expected in the final states that are being searched for in this thesis.

The overall performance of the **ID** depends on the three sub-systems and it can be shown in terms of momentum resolution:

$$\frac{\sigma_{p_T}}{p_T} = 1.6 \pm 0.1\% \oplus \frac{(53 \pm 2) \times 10^{-5}}{\text{GeV}} \times p_T \quad (2.3)$$

measured in [44] using cosmic muons before the addition of the **IBL**. Eq. 2.3 shows that the **ID** has a momentum resolution of $\sim 1.6\%$ at low momenta ($\sim 1 \text{ GeV}$) and of $\sim 50\%$ at 1 TeV.

2.2.3 The Calorimeters

The **ATLAS** Calorimeter system, shown in Figure 2.5, is comprised of two main sub-systems; the **ECAL** and Hadronic Calorimeter (**HCAL**), which are designed to stop and measure the energy of electromagnetic-interacting and hadronic particles respectively. The combination of the two provides full coverage in ϕ and $|\eta| < 4.95$. Particles slow

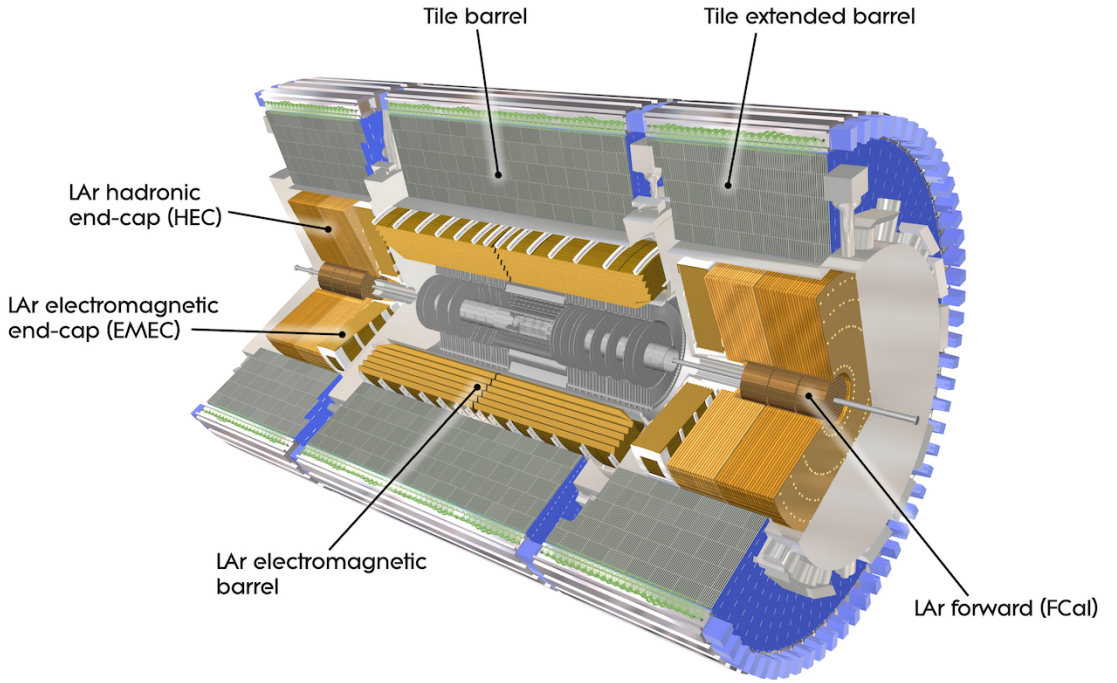


Figure 2.5: A computer generated image of the full calorimeter.

down and lose energy generating showers when crossing different layers. The **ECAL** is comprised of one barrel and two end-cap sectors employing Liquid Argon (**LAr**). The showers hereby develop as electrons pairs which are then collected. The **HCAL** is also comprised of one barrel and two end-cap sectors. The sensors in the barrel of the **HCAL** are tiles of scintillating plastic whereas **LAr** is employed for the end-cap. A forward region, the closest possible to the beam, is covered by a **LAr** forward calorimeter (FCal). The **LAr** and Tile Calorimeter will be briefly discussed in the following paragraphs.

The Liquid Argon Calorimeter

The **ECAL** is comprised of multiple layers of **LAr** sampler and lead absorber. The choice of its accordion-geometry design brought two main advantages; full ϕ coverage with no non-interactive regions (no cracks); fast extraction of signals coming from both front or rear end of the electrodes. It is made of two half-barrel wheels, both placed in the barrel cryostat, that provide a pseudo-rapidity coverage up to $|\eta| < 1.475$ and two end-cap detectors providing $1.375 \leq |\eta| \leq 3.20$ coverage in two end-cap cryostats. The junction between the barrel and end cap components defines the crack region and any signal coming from the crack region is therefore discarded.

In the $|\eta| < 1.8$ region there is an additional layer, placed at the front of the calorimeter, that is made of a thin (0.5 cm in the end-cap and 1.1 cm in the barrel) **LAr** layer

with no absorber [45]. This additional layer was designed to correct for the energy lost, as particles enter the calorimeter, by taking a measurement just before the majority of the electromagnetic shower is developed.

The Tile calorimeter

The main purpose of the hadronic calorimeter is to measure the energy of hadronic showers. It is built employing steel and scintillating tiles coupled to optical fibres which are read out by photo-multipliers. As shown in Figure 2.5, the **HCAL** is made up of three cylinders; a central barrel, 5.64 m long covering a region $|\eta| < 1.0$, and two extended barrel, 2.91 m long covering a region $0.8 < |\eta| < 1.7$. Each cylinder is made up of 64 modules and each module is in turn made up of three layers. Ultimately, the smallest section of the calorimeter module is a cell with a $\Delta\phi \times \Delta\eta = 0.1 \times 0.1$ granularity for the two innermost layers and $\Delta\phi \times \Delta\eta = 0.2 \times 0.1$ for the outermost one.

Performance of the Calorimeter

The performance of the calorimeter is important to measure the properties of the jets used in the analyses presented in this thesis. This has been assessed using test beam data and, once the noise has been subtracted from the experimental measurements these are fit using Eq. 2.4

$$\frac{\sigma(E)}{E} = \frac{a}{\sqrt{E[\text{GeV}]}} \oplus b \quad (2.4)$$

Here, a is the stochastic term and b is a constant that includes local non-uniformities in the calorimeter response.

The **ECAL** performance in the barrel was assessed firing an electron beam at a module that is identical to those in **ATLAS** and the fitted energy resolution is $\sigma(E)/E = (10 \pm 0.4)\%/\sqrt{E} \oplus (0.4 \pm 0.1)\%$ with a variation of no more than 0.7% for the entire coverage of the calorimeter.

The **HCAL** performance in the barrel was assessed firing a pion beam at a prototype detectors of the **LAr** electromagnetic and tile calorimeters. The fitted energy resolution (with an added term to account for electronic noise) is $\sigma(E)/E = (52 \pm 1.0)\%/\sqrt{E} \oplus (3.0 \pm 0.1)\% \oplus (1.6 \pm 0.1)/E$.

2.2.4 The Muon Spectrometer

The **MS** [46], shown in Figure 2.6, is the outermost sub-system of the whole **ATLAS** detector. As such, it surrounds the calorimeters and its main function is to perform precision measurement of muons momenta. The deflection of muon tracks employing large superconducting air-core toroid magnets and high-precision tracking chambers is at the heart of such high precision measurement.

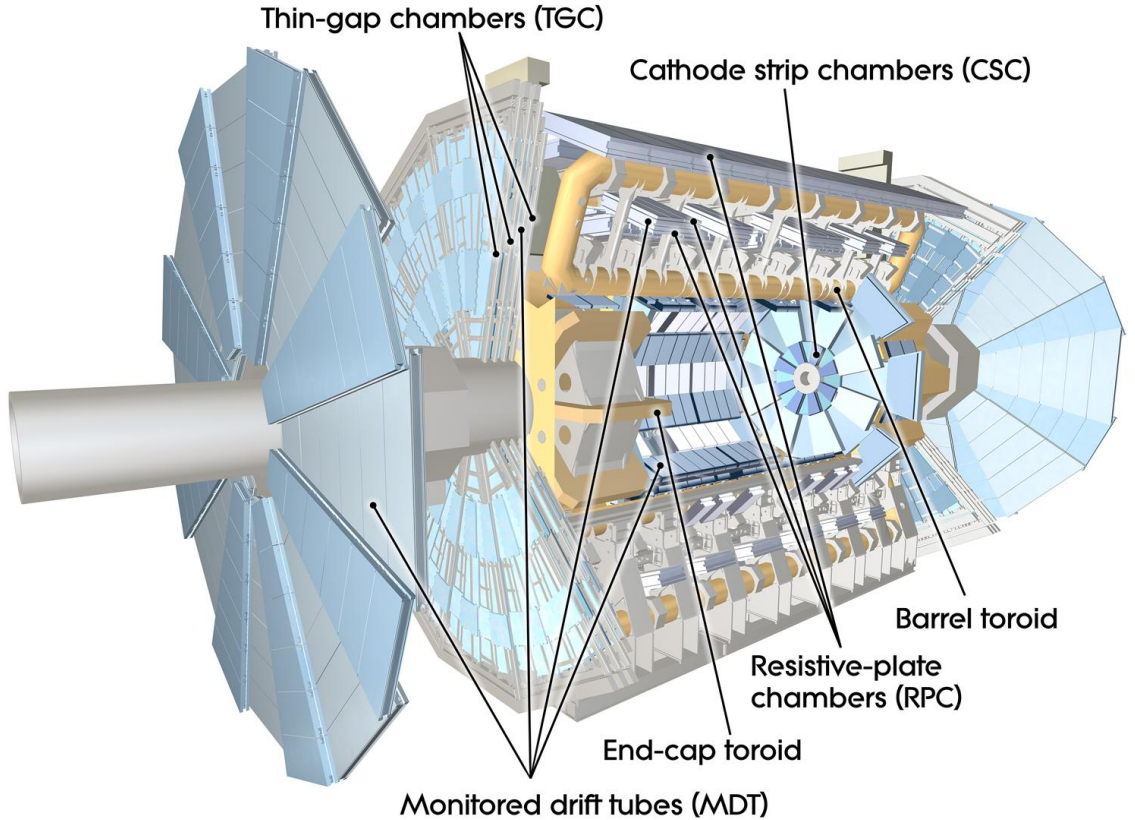


Figure 2.6: Cut-away view of the **ATLAS** muon system [32].

The **MS** is comprised of one large barrel toroid, covering the region $|\eta| \leq 1.4$, and two end-cap toroids, covering $1.6 < |\eta| \leq 2.7$ which are employed together to achieve the track-bending effect wanted. The magnitude of the magnetic field in the barrel, generated by eight large superconducting coils, ranges from 0.5 to 2 T.

Around the beam axis, three cylindrical layers make way for the chambers, placed in planes perpendicular to the beam, used to measure tracks.

Monitored Drift Tubes (**MDTs**) are employed over most of the pseudo-rapidity range to provide precision measurement of track coordinates in the bending direction. An MDT is essentially a set of 30-mm-diameter Aluminium tubes containing a W-Re (Tungsten-Rhenium) wire, surrounded by a non-flammable Ar-CH₄-N₂ mixture at a pressure of 3 bar. The resolution a single wire can give on the particle position is 80 μm enhanced by

having multiple layers of tubes for each module.

Cathode Strip Chambers (**CSCs**) are instead employed at large pseudo-rapidity ($2 < |\eta| < 2.7$). They work similarly to the MDT but instead of tubes there are cathode strips above and below the anode wires. In particular, one set is orthogonal to the wires for precision measurement and the other one parallel to the wires providing a measurement of the transverse coordinate. The gas employed between the strips and wires is a non-flammable mixture of Ar-CO₂-CF₂.

Thin-Gap Chambers (**TGCs**) are employed in the end-cap region and Resistive-Plate Chambers (**RPCs**) in the barrel. The **TGCs** are very similar to the **CSCs**. They provide large signals and in a very narrow time window making them ideal for triggering purposes.

The **RPCs** are also gas-based detectors. They are comprised of two parallel resistive plates held apart by insulating spacers, and a uniform electric field is employed to generate a limited avalanche multiplication centred around the primary ionisation electron. This will then be detected by *Al* strips separated from the plates by an insulating film.

2.3 The ATLAS Trigger System

The **ATLAS** Trigger System is at the heart of data taking. It is an essential component of any nuclear or particle physics experiment as it is responsible for deciding whether or not to store an event for later study. Its main function to reduce the event rate from ~ 40 MHz bunch-crossing³ to ~ 1 kHz.

The Trigger system employs a two-level system: a first hardware-based trigger, Level-1 (**L1**) Trigger, and a software-based, High Level Trigger (**HLT**). **L1** processes low-granularity information from the calorimeter and the muon spectrometer and identifies the so-called Regions of Interest (RoIs)⁴ before making a decision. Event data from other sub-system are temporarily stored in memories whilst **L1** decision is taken.

Further investigations are left to **HLT** which is made of software running on a cluster of computers (**HLT** farm). Additionally, a Fast TracKer (**FTK**) system [47] (to be installed before the end of Run 2) will process events that are accepted by **L1** trigger, and seed the **HLT** algorithms. It will provide global **ID** track reconstruction at the **L1** trigger rate using lookup tables stored in custom associative memory chips for the pattern recognition.

The **ATLAS** trigger system will be further discussed in Chapter 3, however the Run-

³ The term bunch-crossing, $\langle \mu \rangle$, is hereby used when referring to a collision between two bunches of protons.

⁴ $\eta - \phi$ regions where event features have been found by the **L1** selection process.

1-to-Run-2 upgrade of the [ATLAS](#) trigger will not be discussed any further.

3 | The ATLAS Trigger System

*Software is a great combination
between artistry and engineering.*

Bill Gates

The [ATLAS](#) trigger system together with its performance will be presented in this chapter. A brief introduction about the reason behind the need of a trigger system, together with its implementation in [ATLAS](#), will be discussed in Section 3.1. The [L1](#) trigger and [HLT](#) will be discussed in Sections 3.2 and 3.3, respectively. Finally, Section 3.3.2 will be dedicated to the performance of [HLT](#) for low- p_T single-lepton, and medium- and high- p_T b -jet triggers - which has been part of the *qualification task*¹ of the author -, together with the performance of the missing transverse energy trigger, E_T^{miss} , - as the most relevant trigger for the analysis discussed in Chapter 5.

3.1 Overview

More than 80 fb^{-1} of pp collisions were delivered in 2016 and 2017 by the [LHC](#) and, due to storage space limitations, it is not feasible to save all the information about the collision after every bunch crossing, so the [ATLAS](#) Trigger System is indispensable to reduce the read-out rate to a sensible value without affecting the physics programme of [ATLAS](#), e.g. discarding potentially interesting events. A multiple-level architecture is employed to allow the trigger enough time to identify interesting events, using both software- and hardware-based real-time algorithms.

Figure 3.1 shows the Trigger and Data Quality ([TDAQ](#)) system. This is comprised of both a hardware-based first-level trigger ([L1](#)) and a software-based [HLT](#), as already mentioned in Section 2.3. The [L1](#) trigger decision is formed by the Central Trigger Processor ([CTP](#)), which receives inputs from the L1 Calorimeter ([L1Calo](#)) and L1 Muon ([L1Muon](#))

¹ In order to become an [ATLAS](#) author, a person must have been an active [ATLAS](#) member for at least one year working on a technical work

triggers. Once the events pass the L1 selection, they are buffered in the Read-Out System (ROS) and processed by the HLT, which receives information on the Region of Interest (RoI) from L1 to be used for track reconstruction in the trigger algorithms. An RoI is an extended wedge-shaped spatial region in the detector, consisting of a direction in $\eta - \phi$ originating from a z -position along the beam-line, extended along the beam-line by independent directions with respect to this z position, and extended about the ϕ direction with independent directions in pseudo-rapidity, at the maximum and minimum z positions along the beam-line.

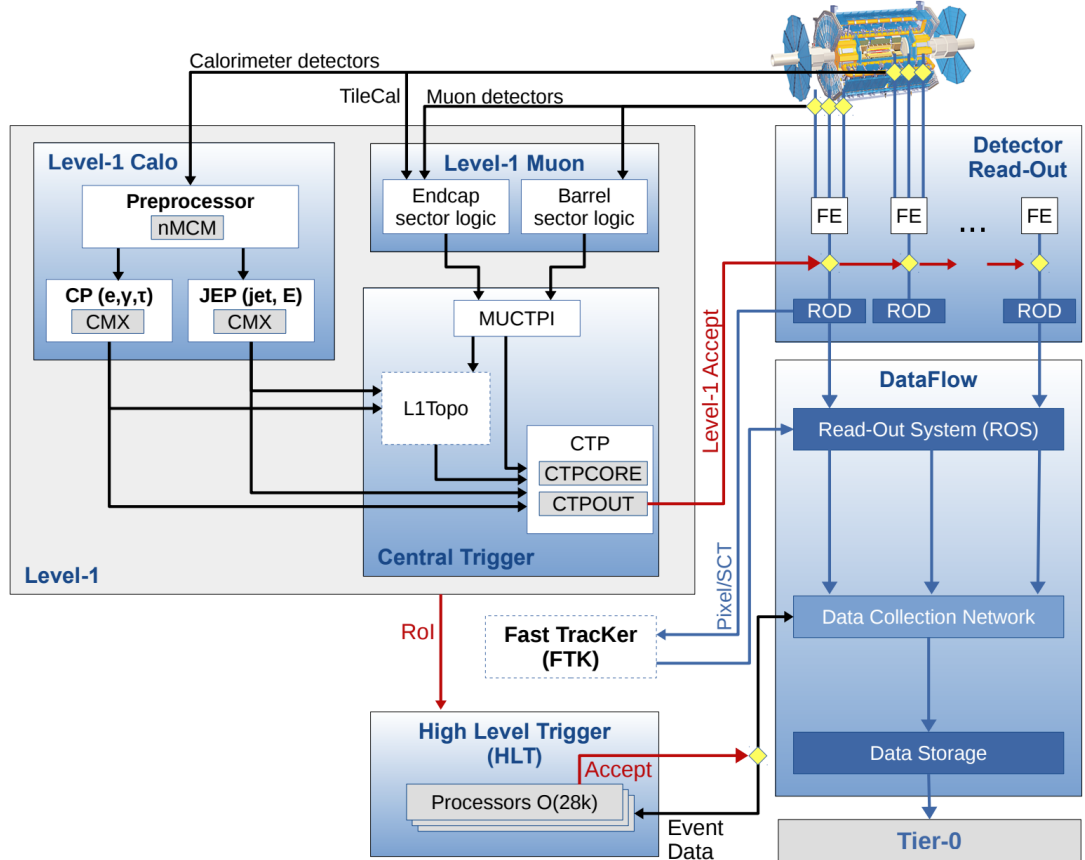


Figure 3.1: The ATLAS TDAQ system. L1Topo and FTK [48] have not been used for the results shown in this thesis.

The trigger system is configured via the so-called trigger *menu* which contains the multiplicity requirement (number of tracks) and the pre-scale factors². Additionally, the menu is meant to define the trigger *chains* - usually referred to just as trigger - that start from a L1 trigger and specify a sequence of reconstruction and selection steps for the specific trigger signatures required in the trigger chain. This is named after the following convention:

² A factor associated with a trigger at each level that indicates what fraction of events, that could pass this trigger selection, is actually accepted.

TriggerLevel_TypeAndThreshold_Identification_Isolation

Here, “TriggerLevel” refers to either [L1](#) or [HLT](#), “TypeAndThreshold” refers to the type of object to trigger on (electron, muon, E_T^{miss} , etc.) and its energy threshold. If any identification and/or isolation criteria are included, these are appended at the end of the name: `HLT_e24_lhmedium` is an electron trigger with a 24 GeV threshold, using “medium” identification criteria, which will be further discussed in Chapter 4.

3.2 Level-1 Trigger

The [L1](#) trigger decision is essentially taken by the [CTP](#), based on the information the [L1](#) calorimeter and [L1](#) muon trigger systems. Additionally, a Level-1 Topological ([L1Topo](#)) trigger³, fed with energy and direction information about the objects found by the [L1Calo](#) and [L1Muon](#) triggers, is employed [32, 48, 49].

The [L1](#) trigger system is implemented in fast custom electronics to keep the decision time around 2.5 μs and its decision is used as a *seed* for [HLT](#).

The L1 Calorimeter Trigger

The [L1Calo](#) trigger [32, 50] is based on inputs from the electromagnetic and hadronic calorimeters within the region $|\eta| < 4.9$. It provides triggers for objects such as electrons/photons, taus, jets, and global transverse energy. Dedicated analogue trigger signals, provided by the [ATLAS](#) calorimeters independently from the signals read out and used at the [HLT](#) and offline, make the [L1Calo](#) trigger decision, which is based on the information from analogue sums of calorimeter elements, called *trigger towers*, instead of using the full granularity of the calorimeter. The trigger towers have a size of approximately $\Delta\eta \times \Delta\phi = 0.1$ in the central part of the calorimeter, $|\eta| < 2.5$, and they get larger and less regular in the forward region. Separate trigger towers are employed for electromagnetic and hadronic calorimeters. Furthermore, two processor systems run the trigger algorithms, once the signals have been digitised: the first, called *cluster processor*, uses the full [L1](#) trigger granularity information in the central region to look for small and localised clusters, which are typical a energy deposit left by an electron, photon or tau; the second, the *jet and energy-sum processor*, uses 2×2 sums of trigger towers (jet elements), to identify jet candidates and form missing transverse energy, E_T^{miss} , and total transverse energy, E_T . As an example, Figure 3.2 shows a sketch of the electron/photon and tau triggers. The trigger algorithm identifies a Region of Interest as a 2×2 trigger tower

³ Two FPGA-based (Field-Programmable Gate Arrays) processor modules

cluster in the electromagnetic calorimeter for which the transverse-energy sum, released in at least one of the four possible pairs of nearest neighbour towers (1×2 or 2×1), exceeds a pre-defined threshold. Additionally, jets RoIs are defined as 4×4 , 6×6 or 8×8 trigger-tower windows for which the summed electromagnetic and hadronic transverse energy exceeds pre-defined thresholds and which surround a 2×2 trigger tower core that is a local maximum that will be also used to define the coordinates of the jet RoI.

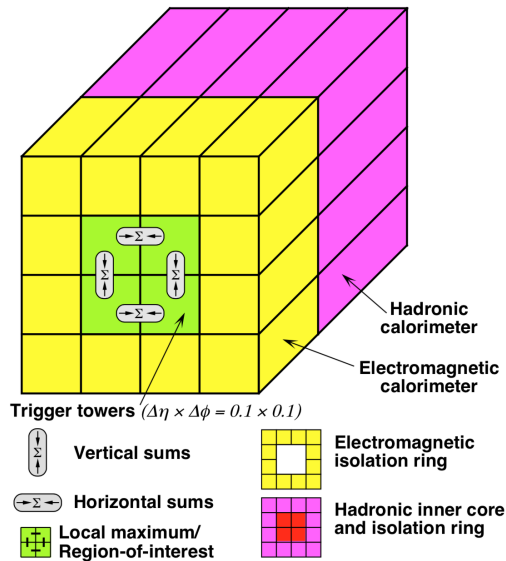


Figure 3.2: Illustration of the electron/photon and tau algorithms with the sums to be compared to programmable thresholds (from [51]).

The L1 Muon Trigger

The L1Muons trigger system [52] processes input data from fast muon trigger sub-detectors and its main task is to select muon candidates with a p_T threshold of 6 GeV and identify the bunch crossing in which they were produced.

Figure 3.3 shows how muons are triggered at L1. The RPC system in the barrel region ($|\eta| < 1.05$) and the TGC system in the end-cap regions ($1.05 < |\eta| < 2.4$) are employed. They provide a rough measurements of muon-candidate p_T , η , and ϕ . Three planes in the barrel and three in each endcap form the trigger chambers. Each plane is comprised of two to four layers and muon candidates are identified by forming coincidences between the muon planes. Coincidences are formed requiring hits that lie within parametrised geometrical muon *roads*. A road, as the example shown in Figure 3.3, essentially contains the trajectories, from the interaction point, of either positively or negatively charged muons with a p_T above a given threshold. In particular six programmable p_T thresholds are employed at L1, divided into two sets: three low- p_T thresholds meant to cover values up to 10 GeV, and three high- p_T thresholds meant to cover $p_T > 10$ GeV.

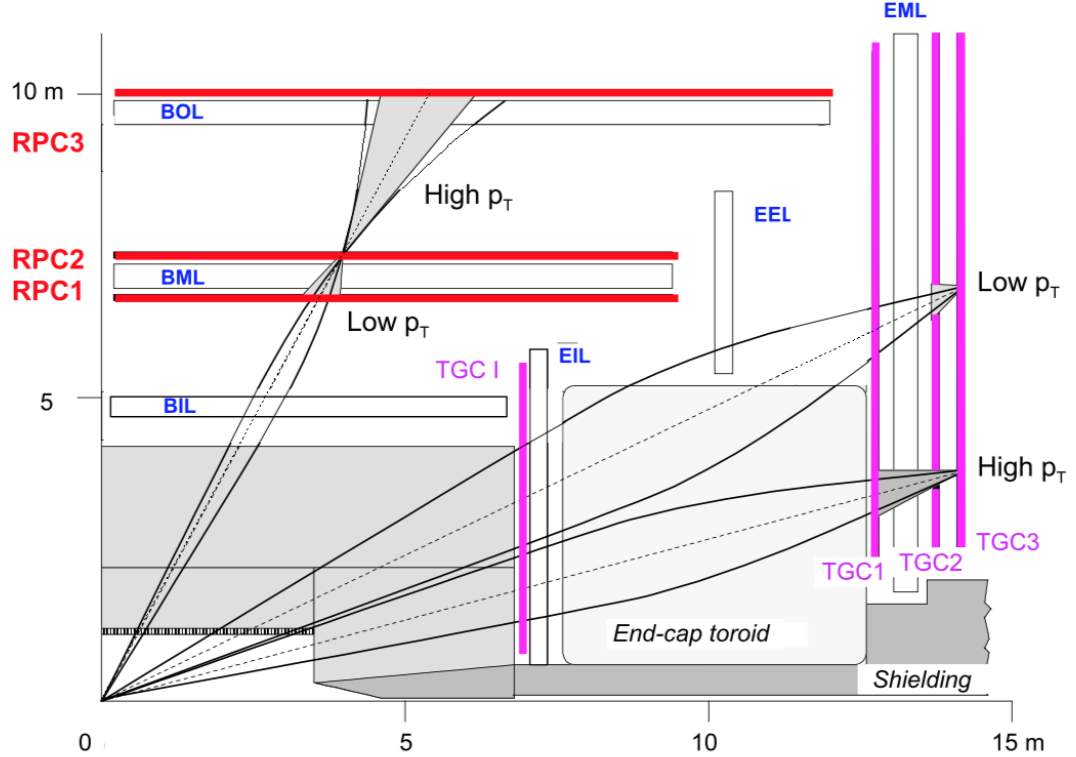


Figure 3.3: A schematic view of the L1Muon trigger chambers (from [51]).

The CTP

The CTP [32] applies the multiplicity requirements and pre-scale factors specified in the trigger menu to the inputs from the L1 trigger systems and forms the L1 trigger decision. Timing and control signals⁴ are employed to distribute the L1 trigger decision to all ATLAS sub-detector readout systems. It is responsible for applying the so-called *preventive dead-time*, meant to limit the minimum time between two consecutive L1 accepts (*simple dead-time*), $\mathcal{O}(100\text{ns})$, in order to both avoid overlapping readout windows, and restrict the number of L1 accepts allowed in a given number of bunch-crossings (*complex dead-time*) to avoid buffers from overflowing. In addition, a *busy dead-time*, can be introduced by ATLAS sub-detectors to temporarily throttle the trigger rate. These dead-times are used to monitor the total L1 trigger rate, and individual trigger rates that need to be monitored before and after any pre-scales and/or any vetoes that have been applied. Furthermore, such information is also used to provide a measure of the L1 dead-time, which has to be accounted for when determining the luminosity [51].

⁴ The timing signals are defined with respect to the LHC bunch crossings: a 25 ns time window centred on the instant at which a proton bunch might cross the ATLAS interaction point.

3.3 High-Level Trigger

The events that are accepted by [L1](#) are then buffered in the [ROS](#) and processed by the *High-Level Trigger* using information that is not available at [L1](#), such as finer-granularity calorimeter inputs, precision measurements from the [MS](#) and tracking information from the [ID](#). [HLT](#) receives [RoI](#) from [L1](#) and performs the reconstruction within them. As needed, the reconstruction performed by the [HLT](#) software can either be run within [RoIs](#) or performing a so-called *full scan* of the detector. In order to reduce the processing time, a two-stage approach is employed for most [HLT](#) triggers: a first reconstruction (fast) to reject the majority of events; a second precision reconstruction for the remaining events (slower). Events that are accepted by the [HLT](#) get transferred to local storage at the experimental site and exported to the CERN’s computing centre for offline reconstruction [48].

3.3.1 Inner detector tracking

The track reconstruction in the Inner Detector is a vital component of the trigger decision in the [HLT](#). A robust reconstruction of particle trajectories is an essential prerequisite for triggering on electrons, muons, taus, and b -jets. Furthermore, it is also used for triggering on inclusive $p\bar{p}$ interactions and for the on-line determination of the beam spot⁵ where the reconstructed tracks provide the input for vertex reconstruction.

The ID tracking in the trigger also includes information from the IBL, which significantly improves the tracking performance and in particular the impact parameter resolution [41]. The tracking algorithms are called *Fast Tracking* and *Precision Tracking*. The former is comprised of trigger-specific pattern recognition algorithms, unlike the latter which is heavily based on offline-tracking algorithms. As already mentioned, once an [RoI](#) has been identified by [L1](#), the algorithms are typically configured to run within it. Furthermore, in order to reduce CPU usage, the offline track-finding is seeded with tracks and space-points identified by fast tracking stage seeds. Running the full [HLT](#) reconstruction for each event on an individual node, affords the opportunity to better optimise the [RoI](#) geometry and use an advanced multi-stage strategy for the tau and b -jet triggers, which will be discussed in Section 3.3.2.

In order to reduce the detector volume of [RoI](#), an advanced multi-stage approach, in particular for tau and b -jet tracking, is employed. The first stage is to identify leading tracks within a long-in- z but narrow-in- η and ϕ [RoI](#) running the Fast Track Finder ([FTF](#)) algorithm. The leading tracks are used to construct a second-stage [RoI](#), constrained in both η and ϕ , but very tightly constrained in polar angle and with a small z position

⁵ The luminous region produced by the collisions of proton beams.

width. The **FTF** is then run again within the wider second-stage **RoI**, followed by the Precision Tracking [48, 53]. The second stage, the Precision Tracking, is heavily based on an optimised subset of the tracking algorithms used offline, which is slower than the first but, in return, it identifies objects constructed starting from the inner detector tracks.

3.3.2 Performance of HLT

The performance of the tracking was estimated using 13-TeV pp collision collected in July 2015 by the **ATLAS** detector, unless otherwise stated. In order to be as unbiased as possible, specific monitoring triggers that do not require a track to be present for the event to be accepted are used to estimate the efficiency of the tracking algorithms. All the quantities used to estimate the performance of the tracking, i. e. efficiencies, residuals and resolutions, are calculated with respect to the tracks found by the offline reconstruction software. In particular, the efficiency is defined as the fraction of offline reference tracks that are matched to a trigger track

$$\mathcal{E} = \frac{N_{\text{trigger}}}{N_{\text{offline}}} \quad (3.1)$$

The tracking efficiency has been estimated for electrons and muons for the single-stage tracking, and for b -jets for the multi-stage approach, as part of the author’s qualification task. The reconstructed tracks are required to have at least two (six) pixel (SCT) clusters and lie in the region $|\eta| < 2.5$. The closest trigger track within a cone of size $\Delta R = \Delta\eta^2 + \Delta\phi^2 = 0.05$ of the offline reconstructed track is selected as the matching trigger track.

Electrons

Figure 3.4 shows the tracking efficiency for the 24 GeV electron trigger as a function of η and p_T of the offline track. The tracking efficiency is measured with respect to off-line tracks with $p_T > 20$ GeV for tight offline electron candidates from the 24 GeV electron support trigger, which does not use the trigger tracks in the selection, despite being identical to the physics trigger. The **FTF** and Precision Tracking efficiencies are all above 99% within the whole pseudo-rapidity range. The small efficiency drop at low p_T is due to bremsstrahlung energy loss by electrons [48].

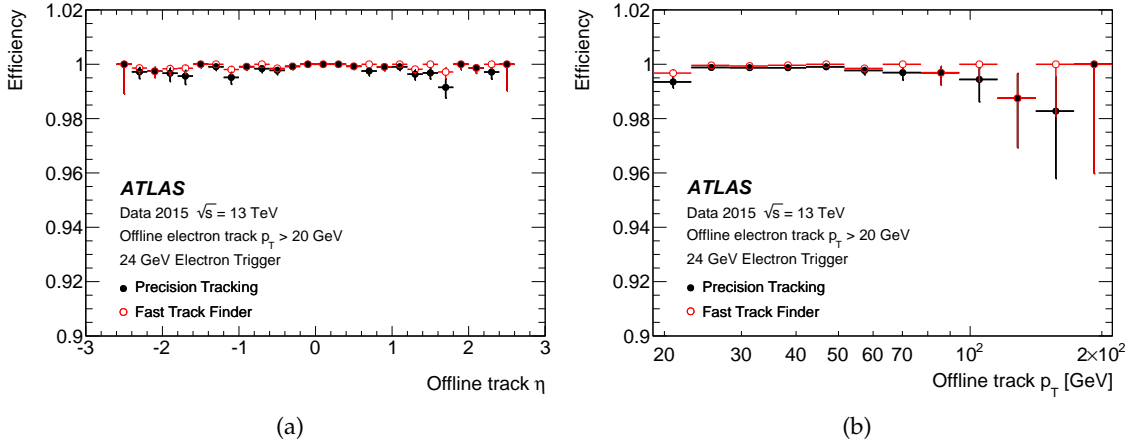


Figure 3.4: The ID tracking efficiency for the 24 GeV electron trigger is shown as a function of the (a) η and (b) p_T of the track of the offline electron candidate. Uncertainties based on Bayesian statistics are shown (from [48]).

Muons

Figure 3.5a shows the muon tracking performance with respect to offline muon candidates with $p_T > 6$ GeV selected by the 6 GeV muon support trigger as a function of the offline muon p_T . The efficiency is well above 99% in the entire p_T range for both FTF and Precision Tracking. Figure 3.5b shows the resolution of the transverse track impact parameter with respect to offline as a function of the offline muon p_T . FTF and Precision Tracking resolutions are better than 17 and 15 μm , respectively, for muon candidates with offline $p_T > 20$ GeV. The difference ($\sim 10\%$) between the two algorithms is driven by the fact that Precision Tracking (black solid points) uses the space points found by the FTF (red open points), but refits them using the offline algorithm. In other words, Precision Tracking runs a faster version of the full offline track fit and it performs better.

b -jets

As previously mentioned, the b -jet triggers tracking algorithms are run in a larger RoI than for electrons or muons and in order to limit CPU usage, multiple stage track reconstruction was implemented and deployed during Run-2.

First, the leading track and its position along the beam-line are determined by executing fast tracking in an RoI that is fully extended along the beam-line, in the $|z| < 225$ mm region, but narrow (0.1) in both η and ϕ , as shown in the blue-shaded region in Figure 3.6. The second stage is then run, using this position along the beam-line, to reconstruct all tracks in an RoI that is larger (0.4) in both η and ϕ but limited to $|\Delta z| < 10$ mm with respect to the leading track, as shown by the green-shaded region in Figure 3.6.

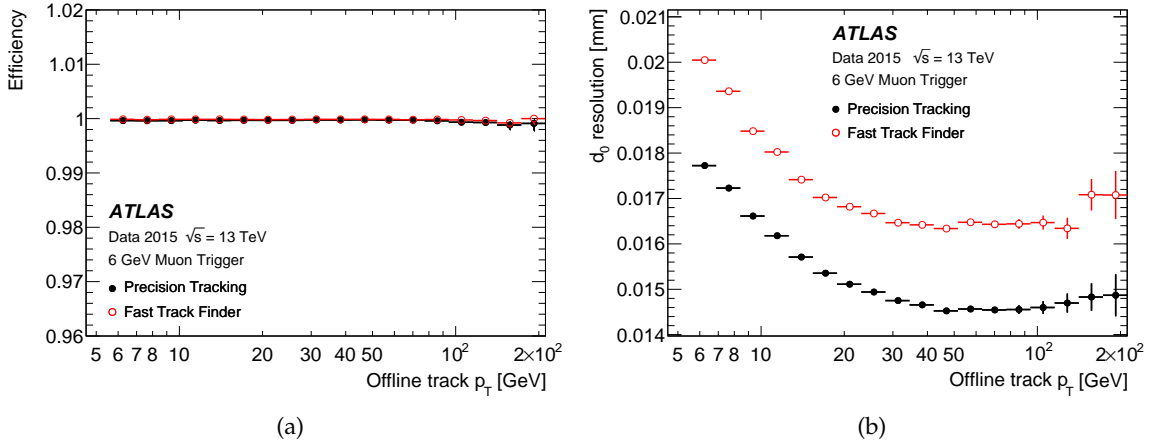


Figure 3.5: The ID tracking performance for the 6 GeV muon trigger; (a) efficiency as a function of the offline reconstructed muon p_T , (b) the resolution of the transverse impact parameter, d_0 as a function of the offline reconstructed muon p_T . Uncertainties based on Bayesian statistics are shown (from [48]).

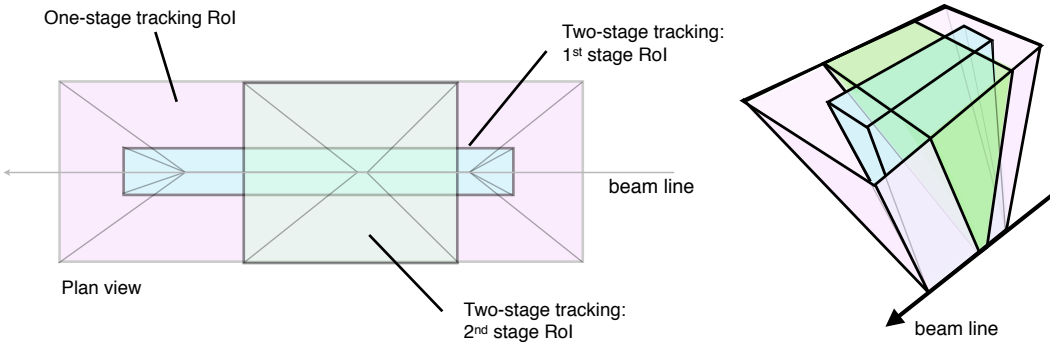


Figure 3.6: An illustration of the RoIs from the single-stage and two-stage tau lepton trigger tracking, shown in plan view (x-z plane) along the transverse direction and in perspective view. The z-axis is along the beam line. The combined tracking volume of the 1st and 2nd stage ROI in the two-stage tracking approach is significantly smaller than the ROI in the one-stage tracking scheme (from [48]).

The first-stage vertex tracking takes all jets identified by the jet trigger with $\eta > 30$ GeV and reconstructs tracks with the FTF in a narrow region in η and ϕ around the jet axis for each jet, but with $|z| < 225$ mm along the beam line.

Following this step, the primary vertex reconstruction [54] is performed using the tracks from the fast tracking stage. This vertex is used to define wider RoIs around the jet axes, with $|\Delta\eta| < 0.4$ and $|\Delta\phi| < 0.4$ but with $|\Delta z| < 20$ mm relative to the primary vertex z position. These RoIs are then used for the second-stage reconstruction that runs the fast track finder in the wider η and ϕ regions followed by the Precision Tracking, secondary vertexing and b -tagging algorithms, which will not be discussed in this work.

The performance of the primary vertexing in the b -jet vertex tracking can be seen in Figure 3.7a, which shows the vertex finding efficiency with respect to offline vertices in

jet events with at least one jet with transverse energy above 55, 110, or 260 GeV and with no additional b -tagging requirement. The efficiency is shown as a function of the number of offline tracks with $p_T > 1$ GeV that lie within the boundary of the wider **RoI** (defined above) from the selected jets. The efficiency rises sharply and is above 90% for vertices with three or more tracks, and rises to more than 99.5% for vertices with five or more tracks. The resolution in z with respect to the offline z position as shown in Figure 3.7b is better than 100 μm for vertices with two or more offline tracks and improves to 60 μm for vertices with ten or more offline tracks.

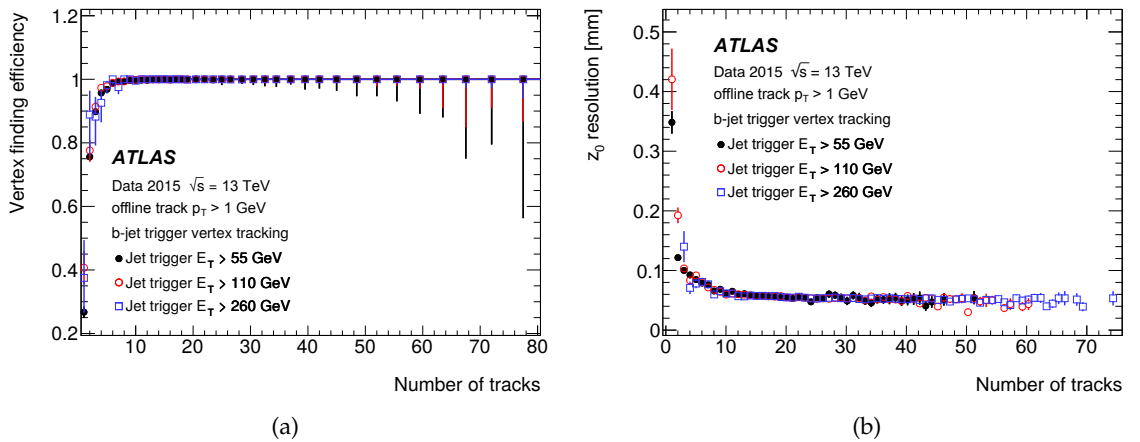


Figure 3.7: The trigger performance for primary vertices in the b -jet signatures for 55, 110 and 260 GeV jet triggers; (a) the vertexing efficiency as a function of the number of offline tracks within the jets used for the vertex tracking, (b) the resolution in z of the vertex with respect to the offline vertex position as a function of the number of offline tracks from the offline vertex (from [48]).

Missing Transverse Energy, $E_{\text{T}}^{\text{miss}}$

There exists several algorithms to reconstruct the $E_{\text{T}}^{\text{miss}}$ at the **HLT**. The *missing H_{T}* ⁶ (MHT) algorithm calculates $E_{\text{T}}^{\text{miss}}$ as the negative sum of transverse energy of calibrated jets, constructed from calibrated topological clusters of calorimeter cells. This algorithm is the most relevant to the analysis presented in Chapter 5. The *cell algorithm* is based on the negative sum of transverse energy deposited in calorimeter cells above a certain noise threshold. Unlike the cell algorithm, which calculates $E_{\text{T}}^{\text{miss}}$ on the electromagnetic scale, the MHT algorithm looks at jets calibrated using jet energy scale, so that numerical threshold values for similar signal efficiencies differ. *Pufit*, a third algorithm, was employed to disentangle calorimeter deposits from the hard-scatter, from those originating from pile-up interactions by grouping towers made out of topological clusters into a pile-up and a hard-scatter category. This grouping is based on their energy, where the threshold itself is dependent on the overall event activity measured by the total energy

⁶ H_{T} is the scalar sum of the various p_{T} s in the event, $H_{\text{T}} = \sum_i p_i^2$.

deposited in the calorimeter. The assumption is that the contribution to E_T^{miss} due to pile-up interactions is zero. Nevertheless a minimisation, which takes into account resolution terms, determines an effective energy density from pile-up interaction which allows a vanishing contribution to E_T^{miss} by the pile-up calorimeter towers. This correction is then subtracted from the hard-scatter towers. The negative sum of transverse energy of those pile-up corrected hard-scatter towers will provide the final E_T^{miss} value [55].

Figure 3.8 shows the turn-on curves for various E_T^{miss} triggers: Figure 3.8a shows the efficiency as a function of *modified*⁷ offline E_T^{miss} for three different E_T^{miss} trigger algorithms, using early 2016 pp collision data. The events have been selected using single lepton (electron or muon) triggers. The x-axis shows the offline E_T^{miss} calculated from the sum of electrons, photons and jets, without the contributions from the muons. Three different E_T^{miss} high-level trigger algorithms are shown: `HLT_xe80_tc_lcw_L1XE50` calculates E_T^{miss} based on calibrated clusters of calorimeter cells, and has a threshold of 80 GeV. `HLT_xe90_mht_L1XE50` calculates E_T^{miss} based on reconstructed jets, and it has a threshold of 90 GeV. `HLT_xe100_L1XE50` calculates E_T^{miss} based on calorimeter cells calibrated at the electromagnetic scale, and has a threshold of 100 GeV. All three algorithms are seeded by a Level-1 trigger algorithm with a threshold of 50 GeV which is also shown; Figure 3.8b shows the combined L1 and HLT efficiency of the missing transverse energy triggers `HLT_xe110_pufit_L1XE50` and `HLT_xe110_mht_L1XE50` as well as the efficiency of the corresponding L1 trigger (`L1_XE50`) are shown as a function of the reconstructed E_T^{miss} (modified to count muons as invisible) using pp collision data collected in 2017. The events shown are taken from data with a $W \rightarrow \ell\nu$ selection to provide a sample enriched in real E_T^{miss} . The HLT E_T^{miss} of the *pufit* algorithm is calculated as the negative of the transverse momentum vector sum of all calorimeter topological clusters corrected for pileup. The pileup correction is done by grouping the clusters into coarser “towers” which are then marked as pileup if their E_T falls below a pileup-dependent threshold.

⁷ To calculate the E_T^{miss} efficiency, e.g. in events with muons, a muon trigger must be employed, therefore muon contributions are removed.

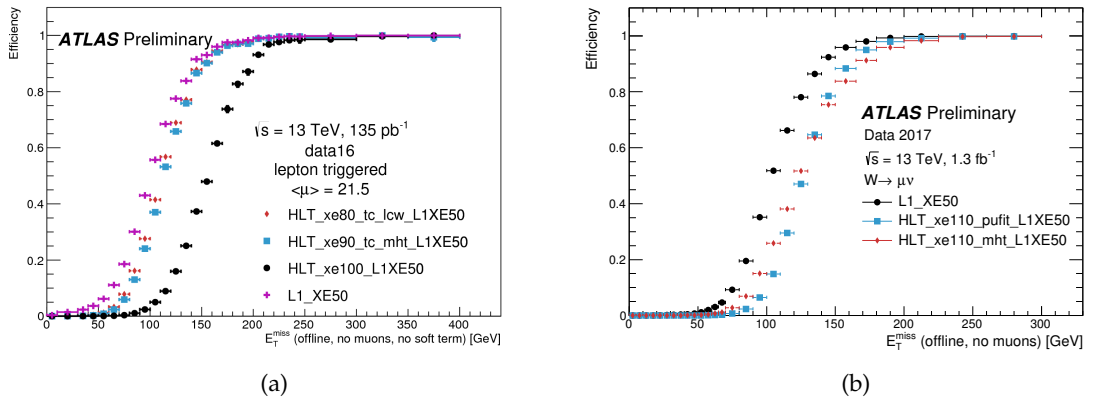


Figure 3.8: Turn-on curves of various E_T^{miss} triggers: Figure 3.8a shows the efficiency as a function of offline E_T^{miss} for three different E_T^{miss} trigger algorithms. Three different E_T^{miss} high-level trigger algorithms are shown: HLT_xe80_tc_lcw_L1XE50 calculates E_T^{miss} based on calibrated clusters of calorimeter cells, and has a nominal threshold of 80 GeV. HLT_xe90_mht_L1XE50 calculates E_T^{miss} based on reconstructed jets, and has a nominal threshold of 90 GeV. HLT_xe100_L1XE50 calculates E_T^{miss} based on calorimeter cells calibrated at the electromagnetic scale, and has a nominal threshold (at the electromagnetic scale) of 100 GeV. All three algorithms are seeded by a Level-1 trigger algorithm with a nominal threshold of 50 GeV which is also shown; Figure 3.8b shows missing transverse energy trigger efficiencies for HLT_xe110_pufit_L1XE50 and for the corresponding L1 seed (L1_XE50). (from [56]).

4 | Event Simulation and Object Reconstruction

Nature isn't classical, dammit, and if you want to make a simulation of nature, you'd better make it quantum mechanical, and by golly it's a wonderful problem, because it doesn't look so easy.

Richard P. Feynman

The [ATLAS](#) software framework Athena [57], which is based on the Gaudi [58] framework developed by [LHCb](#) [34], is used to reconstruct physics objects to be used by analysers, as the data collected and recorded by the [ATLAS](#) detector requires processing. The Athena framework is capable of dealing with various aspects of the experiment software, e. g. triggering or the processing of simulated data. Custom software, in particular Monte Carlo ([MC](#)) simulations, is used to simulate physics events used to model background and signal processes. These are produced through different stages, as shown in Figure 4.1, the last of which produces an analyser-friendly output.

In this chapter the stages will be briefly explained as it follows: event generation (Section 4.1); reconstruction of physics objects¹, in both collected data and simulated [MC](#) events (Section 4.2).

4.1 Generation of a [MC](#)-simulated event

[MC](#) event generators [60] are extensively used in particle physics to simulate [SM](#) and [BSM](#) physics processes. A combination of perturbative and phenomenological calcula-

¹ A set of criteria needs to be applied in order to reconstruct the detected object as an “electron”, “photon”, “muon”, “jet”, etc.

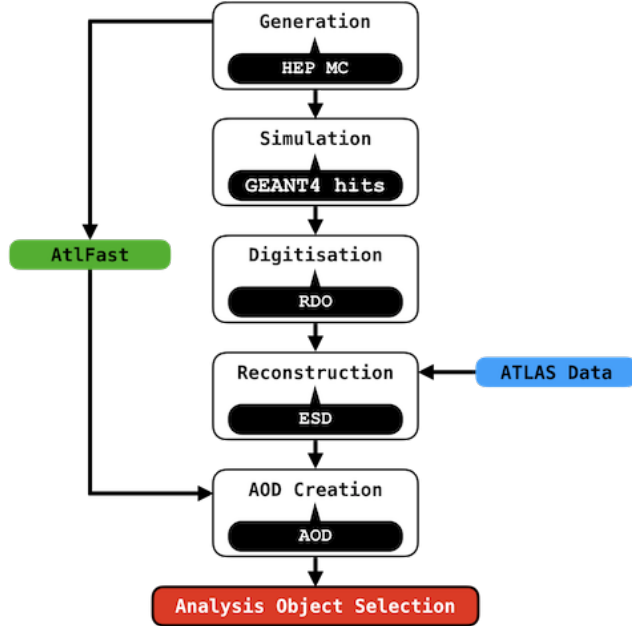


Figure 4.1: Illustration of the different stages of the work flow needed to produce analysable simulated and collected data outputs. The white boxes represent the processes, and their outputs are shown in black balloons: **RDO**, **ESD**, and the final product, **AOD**. The green ‘Atlfast’ box represents the alternative simulation method ATLFAST [59], discussed in Section 4.1. Finally, the blue box shows the stage at which the actual **ATLAS** data events begin processing.

tions, to produce randomly distributed physics events, of a given type, with stable final state particles, is employed. As already mentioned in Chapter 2, The **ATLAS** detector collects $p\bar{p}$ - and heavy-ion-collisions data. When two protons collide at such high energy in the centre of mass, the collision essentially occurs between the nucleon constituents: partons². Three valence quarks (uud), the gluons mediating the strong interactions between the valence quarks, and the sea quarks produced in virtual $q\bar{q}$ pairs due to interacting gluons, are included in the partons. Figure 4.2 shows one of these interactions which are known as Deep Inelastic Scattering (**DIS**) processes, simply because the substructure of the proton is probed, therefore *deep*, by an incoming particle, in this case a proton, whose momentum is not conserved in the process, therefore *inelastic*.

An important, yet simplifying, dimensionless physical quantity is the Bjorken scaling [63], which represents the fraction, x , of the proton momentum carried by an interacting parton. The measure of momentum transfer Q^2 in such events, is related to the momentum transferred by the exchanged boson q by $Q^2 = -q^2$. Parton Distribution Functions (**PDFs**) are used to describe mathematically the parton content of the colliding protons in order to model their interaction.

² “Feynman [61] interpreted the Bjorken scaling as the point-like nature of the nucleon’s constituents when they were incoherently scattered by the incident electron. Feynman named the point-like constituents partons. This is the parton model.”(taken from [62])

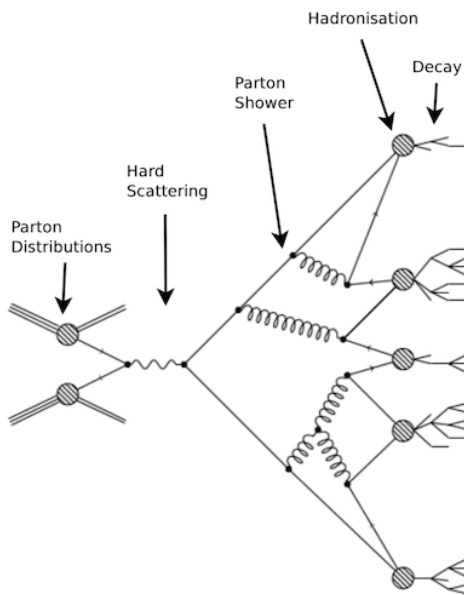


Figure 4.2: Example of a pp DIS event.

The pp scattering at the LHC can be categorised in processes such as *hard*, which can be described with perturbation theory, or *soft*, which involve non-perturbative QCD effects. Typically, a pp collision involves a hard scattering process between two partons, one for each proton, and a certain number of soft processes, such as Initial State Radiation (ISR), Final State Radiation (FSR), and Underlying Event (UE). The ISR involves particles, that are radiated by partons, which will interact in the hard process prior to their scattering. Those partons, which are not involved in the hard scattering process, the so-called *spectators*, form the UE. The FSR refers to particles that are radiated from the final state products of the hard scattering. Furthermore, *parton showering* is a process in which particles in the event that have colour can radiate gluons and/or produce $q\bar{q}$ pairs. Products of these showers will undergo the process of *hadronisation* during which colourless hadron states are produced if Q^2 is of the order of 1 GeV. Such a process occurs due to confinement.

In order to allow analysers to select samples with relevant processes, MC samples are divided in categories depending upon the hard-process specified before generation. It is also possible to filter events to only produce a given final state, e.g. asking for zero leptons, in order not to waste computational resources on events which would not pass any selection criteria, regardless, improving the available statistics. The effect of the selection will be taken into account by applying filter efficiency when the analysis is carried out. The HEPMC format is used to store the output of simulated data outputs [64].

Parton Distribution Function

PDFs [65] mathematically describe the probability density of constituent partons of the interacting protons to have a fraction, x , of the nucleon momentum. They depend upon the parton type such as, valence quark, gluon, or sea quark, and the momentum transfer Q^2 . Although perturbative calculations of the PDFs are not feasible, the DGLAP [66, 67] evolution equations, using a range of hard scattering data from both fixed target and collider experiments, can be used to estimate the dependence as a function of Q^2 for a given parton. In other words, PDFs describe the evolution of the structure functions of quarks and gluons as a function of the running³ strong coupling constant α_s . Figure 4.3 shows the PDFs, calculated with input from HERA and CTEQ at $Q^2 = 10 \text{ GeV}^2$ for up and down valence quarks, gluons, and sea-quarks.

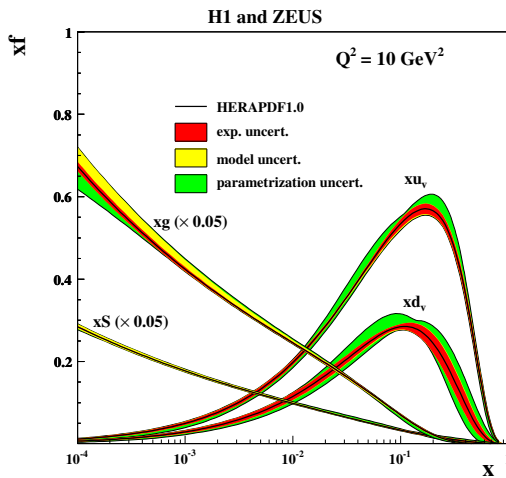


Figure 4.3: PDF from HERAPDF1.0, for up and down valence quarks xu_v and xd_v , gluons xg , and sea quarks $xS = 2x(\bar{U} + \bar{D})$, using a momentum transfer of $Q^2 = 10 \text{ GeV}^2$ (from [68]).

Matrix Element

The matrix element is a simulation stage used to compute the hard processes, where a large momentum transfer ($Q^2 > \mathcal{O}(1 \text{ GeV})$) is involved, which can be calculated using quantum field theory techniques. Matrix elements to Leading Order (LO) or Next-to-Leading Order (NLO) in an expansion in α_s , to calculate a probabilistic distribution of the outgoing partons, are used to make PDFs simulate partons coming into the hard scatter process. Hard emissions, namely the production of high momentum quarks and gluons in the event, therefore processes such as, a gluon splitting into two gluons, $g \rightarrow gg$, or a gluon decaying to a quark-antiquark pair $g \rightarrow q\bar{q}$, and a quark radiating a gluon ($q \rightarrow gq$), can be added into the matrix element.

³ Referred to a dependence on Q^2

Parton Showers

The emission of extra soft objects cannot be modelled with the matrix element, due to its non-perturbative nature. **PS** generators are instead used to include processes such as the emission of a gluon by a quark ($q \rightarrow qg$), or the emission of $q\bar{q}$ pairs $g \rightarrow qq$ or a gluon pair by a gluon $g \rightarrow gg$. HERWIG [69], PYTHIA [70], and SHERPA [71] collaborations have developed the most used **PS** models across the ATLAS community and beyond. Markov chains [72] are the heart of the algorithms used to simulate **PS**. These use probabilities that a gluon is radiated or a $q\bar{q}$ pair is produced.

At intermediate Q^2 , gluon/quark radiation may be treated as a hard emission or part of the **PS**, meaning that, in a given event double-counting might occur. To overcome such issue, the Catani-Krauss-Kuhn-Webber (**CKKW**) [73], and the Michelangelo L. Mangano (**MLM**) [74], schemes are employed to determine whether the emissions are part of the matrix element or **PS**. As the energy of the partons decrease below 1 GeV they will undergo hadronisation.

Hadronisation

As previously mentioned in Section 1.1, once the quarks and gluons in the final state reach a Q^2 of the order of $\Lambda_{\text{QCD}} \sim 200$ MeV, the recombination into colourless objects must occur. The modelling of the production of such bound state, the hadronisation, involves non-perturbative **QCD** and many more parameters than the parton showering. Phenomenological models, tuned using data, are then needed. The cluster model [75], used by HERWIG, and the Lund string model [76], used by PYTHIA, are the most employed.

Underlying Event

Partons not involved in the hard process of the event, referred to as the **UE** [77], can lead to a certain number of soft interactions at a lower energy scale, therefore producing additional hadronic activity in the event. Once again, phenomenological models are used to account for such effect which is modelled within SHERPA and PYTHIA where a whole lot of additional free tuned-to-data parameters are included. More details can be found in [77].

Detector simulation

Although at this stage the output of the **MC** generators contains all the kinematic features of the event, it is not yet possible to compare to the **ATLAS** collected data, as the interactions of the particles passing through the detectors are not yet included. The GEANT4 software [78], included within the **ATLAS** offline software⁴, is used to simulate the energy deposited within the detector: a first stage is run to simulate the interactions of the particles with the various sub-systems, and a second one is run to convert energy deposits into detector-output-like signals (voltage, times, etc.). This is the so-called *digitisation*. The output is now produced with a format that is identical to the one produced by the **ATLAS TDAQ** system, therefore **MC** and collected **ATLAS** data can now be consistently processed by the same trigger and reconstruction software. Nonetheless, the **ATLAS** Collaboration also use faster simulation software such as ATLFast-II (AF2) [59] where, in order to reduce the usage of the available computational resources, a parametrised description of the showers in the calorimeters is implemented.

4.2 Object Reconstruction

At this stage both **MC** and data samples contain all the electronic pulses from the digitisation process. These have to be turned into tracks and calorimeter deposits which, in turn, have to be processed to be reconstructed into physics object, such as electrons, photons, muons, jets, taus, and missing energy, E_T^{miss} . Initially, a set of loose definitions is employed in order for various analyses to use such objects. Later, a set of tighter cuts can be applied depending on what a particular analysis needs to focus on. This approach increases the purity of the selected objects at the expense of selection efficiency. The criteria used to define the physics objects, relevant to the analysis presented in this thesis, will be presented in the following paragraphs.

Tracks and vertices

When a charged particle passes through the detector, all the **ID** sub-systems, pixel, **SCT** and **TRT** components, register “hits” and then, tracing the particle’s trajectory, the hits are reconstructed into a “track”. The most used algorithm is the so-called *inside-out* method, whose clue is in the name: it works outwards from the centre of the **ID** to produce a track once it has initially grouped together hits in the pixel and **SCT** sub-systems. If this track is then compatible with hits in the **TRT** detector, then these hits are also included and the track is accepted. On the contrary, the back-tracking algorithm tries to reconstruct a track

⁴ All the software made available for analysers to be used after the data have been collected

starting from the **TRT** to the **SCT** and Pixel detectors. Tracks can also be reconstructed using only the hits in the **TRT**. A number of selection cuts are applied to the tracks in order to achieve the required quality. Signals produced in other parts of the detector are then used to match **ID** tracks up with charged-particle candidates, e. g. **ECAL** cluster for an electron track. The η and ϕ values are then assigned to tracks using their direction with respect to the origin⁵ in the co-ordinate system described in Section 2.2. The relation that links the p_T of a track to its bending radius and the magnetic field is $p_T = 0.3 \times B \times R$, where the p_T is given in GeV, the magnetic field B in Tesla, and the radius R in meters. Moreover a set of variable is defined:

- d_0 : the distance of closest approach between the track and the origin
- z_0 : the z -plane component of d_0 ;
- $z_0 \sin \theta$: the projection of d_0 onto the z -axis

Vertex reconstruction is needed for various purposes e. g. to differentiate objects from the interesting hard scattering from other pile-up interactions. As the bunch length is finite, pp interactions are spread out in the z coordinate. In order to reconstruct the **PV**, tracks are back-tracked to the beam line. Table 4.1 shows a set of cuts applied to the reconstructed **ID** tracks to be used for vertex reconstruction.

Table 4.1: Cuts applied to the tracks

Variable	Cut
p_T	> 400 MeV
$ \eta $	< 2.5
# IBL hits + B Layer hits	≥ 1
# shared modules ⁶	≤ 1
# Pixel holes ⁷	$= 0$
# SCT holes	≤ 1
# Si ⁸ hits	≥ 9 if $ \eta \leq 1.65$ ≥ 11 if $ \eta > 1.65$

A global maximum in the z coordinate of reconstructed tracks is searched for first, to find a vertex seed. The vertex position is then fitted using an algorithm called the *Adaptive Vertex Fitting* algorithm [79, 80]. The vertex position is determined by fitting to **ID**

⁵ This is assumed to be the position of the primary interaction

⁸ 1 shared Pixel hit or 2 shared **SCT** hits

⁸ Holes exist when a hit is expected in a layer of sensors given the fitted trajectory of the track but none is found

⁸ Silicon refers to IBL, Pixel and SCT

tracks with the least squares fitting method. Outlier tracks⁹ are assigned lower weights in the fit than tracks close to the vertex centre. Outlier tracks have a high probability of being tracks that not originating from another vertex. The adaptive fitting algorithm is able to decrease the sensitivity to these tracks by applying a smaller weight. As we do not know *a priori* the true position of the vertex centre, and which tracks are outliers, the algorithm iteratively tries to fit the vertex: all tracks weights are initialised with high values; after each fit iteration the weight of the outlier tracks is decreased; the algorithm then determines both the vertex centre and which tracks are outliers with increasing accuracy after each iteration; finally, the algorithm will stop once the fitted vertex centre does not change any more. Furthermore, once a vertex is found, tracks which are incompatible with the found vertex will form a new vertex seed. The vertex reconstruction process will terminate once all the tracks have been clustered into vertices or no additional vertices can be found. Among all the vertices found by the algorithm the **PV** will be the one with the highest sum of the squared momenta of the associated tracks (Σp_T^2). The remaining primary vertices found by the algorithm, if any, are referred to as pile-up vertices. Further detail about the algorithm can be found in references [79, 80].

Secondary vertices can also be reconstructed by looking at the displacement, with respect to the primary vertex position, due to the distance travelled by a decaying particle whose lifetime is sufficiently long for the decay length e.g. b-quarks, which travel a few millimetres.

Electrons and Photons

Clusters of energy deposits in the electromagnetic calorimeter are used to reconstruct both electron and photon. The **ECAL** is divided into a grid of towers, each of which measuring $\Delta\eta \times \Delta\phi = 0.025 \times 0.025$. The total tower energy is calculated summing the energy from all longitudinal layers inside each tower. A sliding-window algorithm groups energy towers into electromagnetic (**EM**) clusters [81, 82]. The window width is 3×7 towers in the barrel and 5×5 towers in the endcap. The reconstructed cluster therefore has a size of $\Delta\eta \times \Delta\phi = 0.075 \times 0.175$ in the barrel and 0.125×0.125 in the endcap. In order to achieve better cancellation of systematics when using electrons to measure the photon response, the same window size is employed for electrons and photons [81]. Monte-Carlo-based algorithms and data-driven corrections, derived from $Z \rightarrow ee$ events, are employed to carry out energy calibration [81]. Figure 4.4 shows an illustration of the electron reconstruction algorithm.

Identified clusters are then matched to reconstructed **ID** tracks (required to have a minimum number of pixel and silicon hits) using the track and cluster position. A cluster

⁹ Tracks that are far from the vertex centre

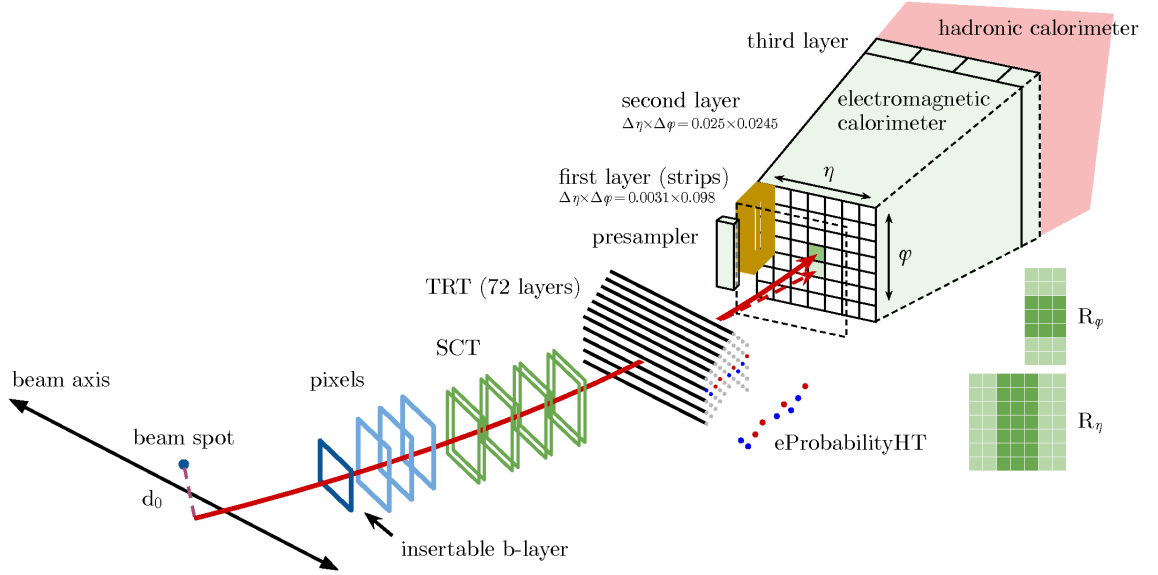


Figure 4.4: Schematic view of the electron reconstruction and identification (taken from [83]).

will be either considered as an electron or a photon candidate, if it satisfies one of the following criteria:

electron: one single reconstructed ID track with an associated vertex;

unconverted photon: no ID tracks;

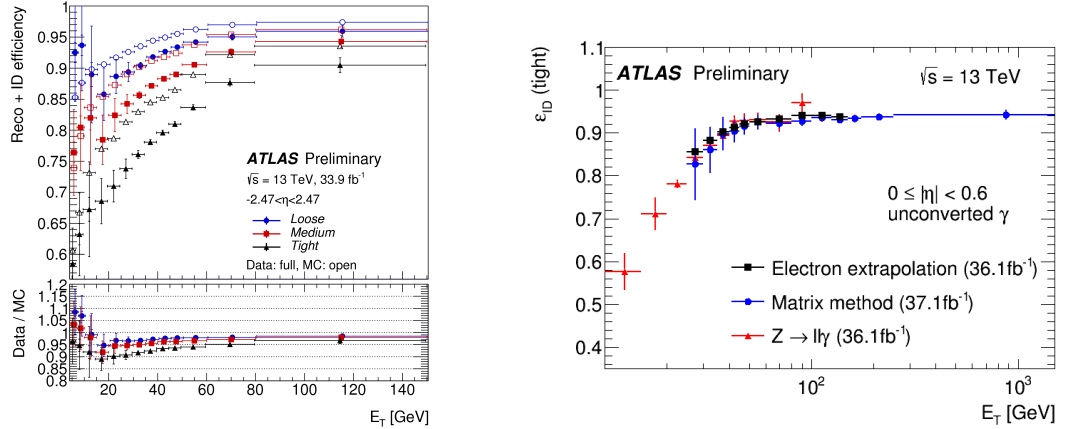
converted photon: two opposite-signed collinear tracks (consistent with electrons) are associated with a secondary vertex;

converted photon: single track is present but there are missing hits in the IBL

Once electrons and photons have been reconstructed an additional set of criteria is employed to rule out any potential misidentification. In particular, the identification is based on a Likelihood (LH) algorithm that depends on variables such as shower shape, radiation deposited in the TRT, and associated-track properties. Identification Working Points (WPs), such as Loose, Medium and Tight, are employed to identify electrons using different selections, which will reflect in different efficiencies and purities¹⁰, as the tighter the identification is, the purer the selected object will be. Figure 4.5 shows the reconstruction and identification efficiencies using 2016 data for electrons, and 2015 + 2016 for unconverted photons. Here, the data-MC discrepancy in the electron identification performance is due to a mismodelling of the TRT conditions in addition to the known mismodelling of calorimeter shower shapes in the GEANT4 detector simulation [84]. Nonetheless, scale factors¹¹ were derived and applied to the Monte Carlo, to match the performance observed in the data.

¹⁰ The number of actual electrons (photons) among the selected candidates.

¹¹ Calibration factors derived from data.



(a) Electron reconstruction and identification efficiencies in $Z \rightarrow ee$ events as a function of E_T , integrated over the full pseudo-rapidity range. The data efficiencies are obtained by applying data/MC efficiency ratios that were measured in $J/\psi \rightarrow e^+e^-$ and $Z \rightarrow ee$ events to MC simulation. The total statistical and systematic uncertainty is shown.

(b) Photon identification efficiencies using the full 2015+2016 dataset Comparison of the data-driven measurements (radiative Z decay, electron extrapolation and matrix method [85]) of the identification efficiency for unconverted photons as a function of E_T in the region $10 \text{ GeV} < E_T < 1500 \text{ GeV}$ for the pseudo-rapidity interval $|\eta| < 0.6$. The error bars represent the sum in quadrature of the statistical and systematic uncertainties estimated in each method.

Figure 4.5: Electron and photon reconstruction and identification efficiencies (taken from [84]).

The shower shape and the amount of hadronic activity behind the **EM** cluster are at the heart of photon identification. The **EM** showers originating from photons and those originating from neutral mesons e.g. π_0 can be distinguished by looking at the energy deposited in the cells within the first and second layer of the **ECAL** [86]. Two categories of photons are reconstructed employing two identification **WPs**: **Loose** and **Tight**. The former are typically used for triggering, the latter for physics analysis, such as the one presented in Chapter 5, where, the top-quark pair production in association with a photon, $t\bar{t}+\gamma$ was studied.

Muons

Two independent track fits in the **ID** and **MS** are the basis of the muons selection procedure. Depending on the signature in each sub-system the fits are combined using different algorithms. Various categories of muons can be reconstructed with the **ATLAS** detector [87] and they can be listed as it follows:

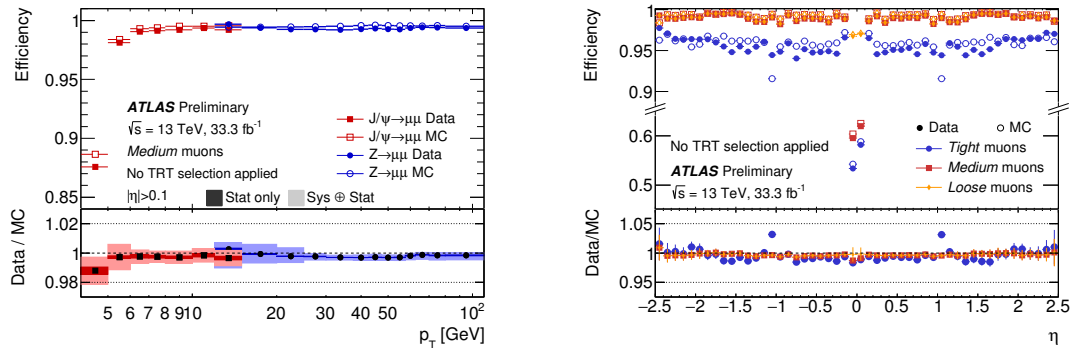
Combined: candidates whose tracks are found in both **ID** and **MS** on which a global refit is run to obtain a combined muon track that describes the trajectory of the

particle through the whole detector, in order to take into account the energy loss in the calorimeter;

Extrapolated: candidates in the forward region ($2.5 < |\eta| < 2.7$) that produced a track in the **MS** but fell outside the **ID** acceptance, therefore their trajectory is reconstructed using the **MS** track, loosening its compatibility requirement with the interaction point;

Segment tagged: candidates whose tracks in the **ID** are found to have a corresponding hit in the inner layer of the **MS**. Generally for muons with low p_T or due to cracks in the **MS**;

Calorimeter tagged: candidates, whose **ID** tracks can be matched with an energy deposit in the calorimeter, compatible with the signature of a Minimum Ionising Particle (**MIP**), with no associated **MS** tracks; mainly muons in the central pseudo-rapidity region ($|\eta| < 0.1$) due to a crack in the barrel of the **MS**;



(a) Muon reconstruction efficiencies for the Medium identification algorithm measured in $J/\psi \rightarrow \mu\mu$ and $Z \rightarrow \mu\mu$ events as a function of the muon p_T . The prediction by the detector simulation is depicted as empty circles (squares), while the full circles (squares) indicate the observation in collision data for $J/\psi \rightarrow \mu\mu$ ($Z \rightarrow \mu\mu$) events. Only statistical errors are shown in the top panel. The bottom panel reports the efficiency scale factors. The darker error bands indicate the statistical uncertainty, while the lighter bands indicate the quadratic sum of statistical and systematic uncertainties.

(b) Muon reconstruction efficiencies for the Loose/Medium/Tight identification algorithms measured in $Z \rightarrow \mu\mu$ events as a function of the muon η for muons with $p_T > 10$ GeV. The prediction by the detector simulation is depicted as open circles, while filled dots indicate the observation in collision data with statistical errors. The bottom panel shows the ratio between expected and observed efficiencies, the efficiency scale factor. The errors in the bottom panel show the quadratic sum of statistical and systematic uncertainty.

Figure 4.6: Muon reconstruction and identification efficiencies (taken from [88]).

In order to separate prompt muons from backgrounds such as pions and kaons decays, further identification requirements are employed, e.g. track quality requirements

in the **ID** and the **MS**, normalised χ^2 of the combined track fit, etc.).

Figure 4.6 shows reconstruction and identification efficiencies as a function of p_T and η . Likewise electrons and photons, in order to meet all the different requirements of the various **ATLAS** analyses, a set of **WPs** is defined. The performance is calibrated using the so-called tag-and-probe method¹² in $Z \rightarrow \mu\mu$ or $J/\psi \rightarrow \mu\mu$ events. Further details can be found at [87].

Jets

As already mentioned in Sections 1.1 and 4.1, due to **QCD** confinement when a pp collision occurs, a spray of hadronic matter, or *jet*, is produced. A jet in the **ATLAS** detector looks like an object that released its energy in both **ECAL** and **HCAL** via **EM** and hadronic showers and, as it is generally comprised of a certain number of charged particles, it also has **ID** tracks associated with the showers. The identification and the reconstruction of jets is important for the analysis discussed in Chapter 5, which targets the $pp \rightarrow \tilde{t}\tilde{t} \rightarrow bqq\tilde{\chi}_1^0 + \bar{b}\bar{q}\bar{q}\tilde{\chi}_1^0$ channel where all the visible decay products are quarks, therefore jets. A brief description of jet reconstruction and calibration is presented in the following paragraphs.

The three-dimensional structure of topological clusters in the calorimeters is used to measure the energy deposited by the showers through the clusters[90, 91]. These are built up via an iterative algorithm which first forms the core of the cluster by identifying seed cells, with a high energy threshold, and adding adjacent cells with a lower threshold, and then, in order to account any potential shower leak an extra layer of cells is added, such that a collection of topological clusters per event is obtained. Jet-finding algorithms, which treat jets as massless objects, are then fed with such clusters information such as energy and position. The former is calculated as the sum of all the energy deposits in the cells previously identified, whose position within the detector is used to deduct angular information. A widely used algorithm within the **ATLAS** Collaboration is the anti- k_t one which forms a collection of jets as output by iteratively recombining the input clusters. The algorithm essentially groups two object into a single one according to a distance d_{ij} , defined as:

$$d_{ij} = \min \left(k_{t_i}^{2p}, k_{t_j}^{2p} \right) \frac{\Delta_{ij}^2}{R^2} \quad (4.1)$$

where i and j are topological cluster indices, k_t is the transverse momentum of each topological cluster, $\Delta_{ij}^2 = \Delta\phi_{ij}^2 + \Delta\eta_{ij}^2$ is the distance between the two topological clusters, and

¹² Method used to select, from known resonances such as $Z \rightarrow ee$ unbiased samples of electrons (probes) by using strict selection requirements on the second object produced from the particle's decay (tags) [89].

R is an input parameter into the algorithm which, in the analysis presented in this work, is set to $R = 0.4$. The topological clusters i and j which minimise d_{ij} are then combined to form larger individual clusters. The next iteration takes into account the larger individual clusters as well as the remaining initial topological clusters and combines them according to the same procedure, which is repeated until all remaining topological-cluster pairs satisfy $\Delta_{ij} > R$. Additional information can be found at [92].

Due to the compensation condition¹³ the hadronic component of the shower produced by jets is underestimated and for such reason a calibration procedure is employed. In particular, the so-called Electromagnetic + Jet Energy Scale scheme is employed [93] where a set of corrections is applied to match the energy of the initial partons. These are **vertex correction**: once the anti- k_t algorithm has reconstructed the jets, its four-vectors, initially pointing at the centre of the detector, are adjusted to point to the primary vertex; **pileup correction**: pileup effect on the jets energy is reduced by using an area-based subtraction procedure [94]; **jet energy and η correction**: additional calibration based on energy and pseudo-rapidity corrections where the kinematical properties of the reconstructed jet (p_T and η) are compared to the ones derived from MC simulations; **global sequential correction**: individual jet property-based correction for properties such as the fraction of energy deposited in different calorimeter layers or the number and type of associated tracks [95]; **in-situ corrections**: then measured p_T of the jet is corrected using multi-jet and $\gamma/Z+jets$ events, where the momentum of a *probe* jet is balanced against a well-measured reference object [96].

Finally, the Jet vertex Tagger (JVT) variable [97], related to the fraction of charged tracks within the jets that point to the primary vertex, is employed. This observable tests the compatibility between the reconstructed jet and the hard-scatter charged particles within the jet [98].

b-tagged jets

The identification and the reconstruction of jets originated from b -quarks is also important, as they also are part of the final state of the analysis presented in this work. Not only is this crucial for this work but also for other analyses carried out by the ATLAS Collaboration. The standard jet-reconstruction procedure discussed above applies to b -jets too, with the addition of dedicated algorithms (b -tagging [99]) employed to spot a b -hadron within their cone. A diagram, showing what the difference between light jets and b -jets, is shown in Figure 4.7. Due to their lifetime of the order of 10^{-12} s, b -hadrons can travel a measurable distance in the detector before decaying, yielding a secondary vertex within

¹³Calorimeters response can be described in terms of the EM/Hadronic ratio, as it is a measure of the calorimeter response to EM VS hadronic radiation. An ideal calorimeter would have EM/Hadronic ~ 1 .

the jet cone. In addition, the impact parameter of the tracks from the b-hadron decay is expected to differ from zero, providing a useful tool for jet flavour discrimination.

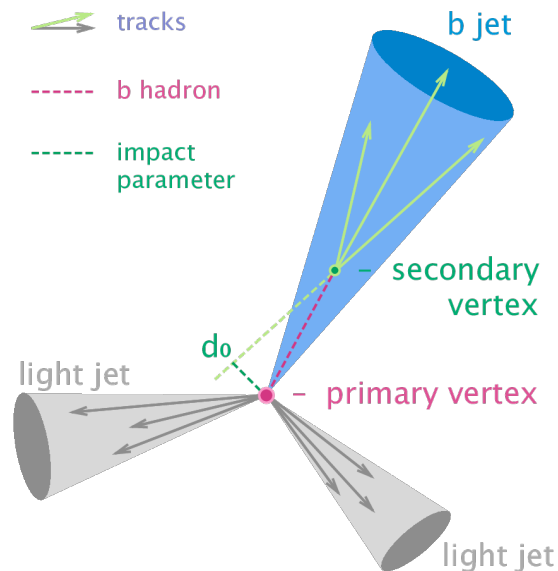


Figure 4.7: Diagram showing the common principle of identification of jets initiated by b -quark decays [100].

Missing Transverse Energy

4.3 Object Selection

4.3.1 Baseline Object Selection

Leptons

Photons

Jets

4.3.2 Overlap Removal

4.3.3 Signal Object Selection

Leptons

Photons

Jets

5 | Stop searches in final states with jets and missing transverse energy

In God we trust. All others must bring data.

W. Edwards Deming

6 | Results and Statistical Interpretations

Conclusion

Last thing to write

Appendix title

List of Acronyms

ALICE A Large Ion Collider Experiment

AOD Analysis Objects Data

ATLAS A Toroidal LHC ApparatuS

BSM Beyond Standard Model

CERN European Organization for Nuclear Research

CKKW Catani-Krauss-Kuhn-Webber

CMS Compact Muon Solenoid

CSC Cathode Strip Chamber

CTP Central Trigger Processor

DIS Deep Inelastic Scattering

DM Dark Matter

ECAL Electromagnetic Calorimeter

EM electromagnetic

ESD Event Summary Data

FCNC Flavour Changing Neutral Currents

FSR Final State Radiation

FTF Fast Track Finder

FTK Fast TracKer

GUT Grand Unification Theory

HCAL Hadronic Calorimeter

HLT High Level Trigger

IBL Insertable B-Layer

ID Inner Detector

ISR Initial State Radiation

JVT Jet vertex Tagger

L1 Level-1

L1Calo L1 Calorimeter

L1Muon L1 Muon

L1Topo Level-1 Topological

LAr Liquid Argon

LEIR Low Energy Ion Ring

LEP Large Electron-Positron Collider

LH Likelihood

LHC Large Hadron Collider

LHCb Large Hadron Collider Beauty

LHCf Large Hadron Collider forward

LINAC2 Linear Accelerator 2

LINAC3 Linear Accelerator 3

LO Leading Order

LS1 Long Shut down 1

LSP Lightest Supersymmetric Particle

MC Monte Carlo

MDT Monitored Drift Tube

MIP Minimum Ionising Particle

MLM Michelangelo L. Mangano

MoEDAL Monopole & Exotics Detector At the [LHC](#)

MS Muon Spectrometer

MSSM Minimal Supersymmetric Standard Model

NLO Next-to-Leading Order

NLSP Next Lightest Supersymmetric Particle

PDF Parton Distribution Function

pMSSM Phenomenological [MSSM](#)

PS Parton Shower

PS Proton Synchrotron

PSB Proton Synchrotron Booster

PV Primary Vertex

QCD Quantum Chromodynamics

QED Quantum Electrodynamics

QFT Quantum Field Theory

RDO Raw Data Object

RoI Region of Interest

ROS Read-Out System

RPC Resistive-Plate Chamber

SCT SemiConductor Tracker

SM Standard Model

SPS Super Proton Synchrotron

SUSY Supersymmetry

SV Secondary Vertex

TDAQ Trigger and Data Quality

TGC Thin-Gap Chamber

TOTEM TOTal cross section, Elastic scattering and diffraction dissociation
Measurement at the [LHC](#)

TRT Transition Radiation Tracker

UE Underlying Event

VEV Vacuum Expectation Value

WIMP Weakly Interacting Massive Particle

WP Working Point

Bibliography

- [1] M. Herrero, *The Standard Model*, <https://arxiv.org/abs/hep-ph/9812242>.
2
- [2] ATLAS Collaboration, *Observation of a New Particle in the Search for the Standard Model Higgs Boson with the ATLAS Detector at the LHC*, *Phys.Lett.* **B716** (2012), [arXiv:1207.7214 \[hep-ex\]](https://arxiv.org/abs/1207.7214). 2
- [3] CMS Collaboration, *Observation of a new boson at a mass of 125 GeV with the CMS experiment at the LHC*, *Phys.Lett.* **B716** (2012), [arXiv:1207.7235 \[hep-ex\]](https://arxiv.org/abs/1207.7235). 2
- [4] M. E. Peskin, D. V. Schroeder, *An Introduction to Quantum Field Theory*. Westview Press, 1995. 3
- [5] W. N. Cottingham and D. A. Greenwod, *An introduction to the standard model*. Cambridge, 1998. 3
- [6] L. Lederman and C. Hill, *Symmetry and the Beautiful Universe*. Prometheus Books, 2004. <https://books.google.co.uk/books?id=X2QPAQAAMAAJ>. 3
- [7] A. Pich, *The Standard Model of Electroweak Interactions*, [arXiv:1201.0537 \[hep-ph\]](https://arxiv.org/abs/1201.0537). 4, 7
- [8] K. A. Olive at al. (Particle Data Group), *Review of Particle Physics*, *Chin.Phys. C* **38(9)** (2014). 4
- [9] S. Weinberg, *The quantum theory of fields. Vol. 2: Modern applications*. Cambridge University Press, 2013. 5
- [10] S. L. Glashow, *Partial Symmetries of Weak Interactions*, *Nucl. Phys.* **22** (1961) 579–588. 6
- [11] A. Salam and J. Ward, *Electromagnetic and weak interactions*, *Physics Letters* **13 no. 2, (1964) 168 – 171. <http://www.sciencedirect.com/science/article/pii/0031916364907115>. 6**

- [12] S. Weinberg, *A Model of Leptons*, *Phys. Rev. Lett.* **19** (1967) 1264–1266.
<https://link.aps.org/doi/10.1103/PhysRevLett.19.1264>. 6
- [13] P. W. Higgs, *Broken Symmetries and the Masses of Gauge Bosons*, *Phys. Rev. Lett.* **13** (1964) 508–509. 7
- [14] J. Goldstone, A. Salam and S. Weinberg, *Broken Symmetries*, *Phys. Rev.* **127** (1962) 965–970. 8
- [15] ATLAS Collaboration, “Summary plots from the atlas standard model physics group.” https://atlas.web.cern.ch/Atlas/GROUPS/PHYSICS/CombinedSummaryPlots/SM/ATLAS_a_SMSummary_TotalXsect/ATLAS_a_SMSummary_TotalXsect.png. 10
- [16] S. Weinberg, *Implications of Dynamical Symmetry Breaking*, *Phys. Rev.* **D19** (1976) 1277–1280. 9, 10
- [17] Super-Kamiokande Collaboration, Y. Fukuda et al., *Evidence for oscillation of atmospheric neutrinos*, *Phys. Rev. Lett.* **81** (1998) 1562–1567,
[arXiv:hep-ex/9807003 \[hep-ex\]](https://arxiv.org/abs/hep-ex/9807003). 10
- [18] SNO Collaboration, *Measurement of the Rate of $\nu_e + d \rightarrow p + p + e^-$ Interactions Produced by 8B Solar Neutrinos at the Sudbury Neutrino Observatory*, *Phys. Rev. Lett.* **87** (2001). 10
- [19] T. O. W. of the Nobel Prize. https://www.nobelprize.org/nobel_prizes/physics/laureates/2015/. 10
- [20] E. Kh. Akhmedov, et. al, *Seesaw mechanism and structure of neutrino mass matrix*, *Phys. Lett.* **B478** (1999). 11
- [21] V. C. Rubin and W. K. Ford, Jr., *Rotation of the Andromeda Nebula from a Spectroscopic Survey of Emission Regions*, *Astrophysical Journal* **159** (1970) 379. 11
- [22] M. H. Jones, R. J. A. Lambourne, and S. Serjeant, *An Introduction to Galaxies and Cosmology* (2nd ed). Cambridge University Press/Open University, Cambridge, January, 2015. <http://oro.open.ac.uk/44361/>. 11
- [23] S. P. Martin, *A Supersymmetry primer*, [arXiv:hep-ph/9709356 \[hep-ph\]](https://arxiv.org/abs/hep-ph/9709356).
[Adv. Ser. Direct. High Energy Phys.18,1(1998)]. 11
- [24] R. Barbieri and G. F. Giudice, *Upper Bounds on Supersymmetric Particle Masses*, *Nucl. Phys.* **B306** (1988) 63–76. 11
- [25] F. Jegerlehner, *The hierarchy problem of the electroweak Standard Model revisited*, [arXiv:1305.6652 \[hep-ph\]](https://arxiv.org/abs/1305.6652). 13

-
- [26] H. E. Haber and G. L. Kane, *The Search for Supersymmetry: Probing Physics Beyond the Standard Model*, Phys. Rept. **117** (1985) 75–263. 15
- [27] K. Hidaka and A. Bartl, *Impact of bosonic decays on the search for the lighter stop and sbottom squarks*, Phys. Lett. **B501** (2001) 78–85, arXiv:hep-ph/0012021 [hep-ph]. 15
- [28] C. Borschensky, M. Krämer, A. Kulesza, M. Mangano, S. Padhi, T. Plehn, and X. Portell, *Squark and gluino production cross sections in pp collisions at $\sqrt{s} = 13, 14, 33$ and 100 TeV*, Eur. Phys. J. **C74** no. 12, (2014) 3174, arXiv:1407.5066 [hep-ph]. 18
- [29] O. S. Brüuning, P. Collier, P. Lebrun, S. Myers, R. Ostojic, J. Poole and P. Proudlock, *LHC Design Report*, <https://cds.cern.ch/record/782076>. 20, 22
- [30] J.M. Jowett, M. Schaumann, R. Alemany, R. Bruce, M. Giovannozzi, P. Hermes, W. Hofle, M. Lamont, T. Mertens, S. Redaelli, J. Uythoven, J. Wenninger, *The 2015 Heavy-Ion Run of the LHC*, <http://accelconf.web.cern.ch/accelconf/ipac2016/papers/tupmw027.pdf>. 21
- [31] C. Lefèvre, *The CERN accelerator complex*, <http://cds.cern.ch/record/1260465>. 22, 23
- [32] ATLAS Collaboration, *The ATLAS experiment at the CERN Large Hadron Collider*, Journal of Instrumentation **3** no. 08, (2008) S08003. <http://stacks.iop.org/1748-0221/3/i=08/a=S08003>. 22, 25, 31, 36, 38
- [33] CMS Collaboration, *The CMS experiment at the CERN LHC*, Journal of Instrumentation **3** no. 08, (2008) S08004. <http://stacks.iop.org/1748-0221/3/i=08/a=S08004>. 22
- [34] LHCb Collaboration, et. al, *The LHCb Detector at the LHC*, JINST (2008). 22, 46
- [35] ALICE Collaboration, *The ALICE experiment at the CERN LHC*, Journal of Instrumentation **3** no. 08, (2008) S08002. <http://stacks.iop.org/1748-0221/3/i=08/a=S08002>. 22
- [36] T. T. Collaboration, *The TOTEM Experiment at the CERN Large Hadron Collider*, Journal of Instrumentation **3** no. 08, (2008) S08007. <http://stacks.iop.org/1748-0221/3/i=08/a=S08007>. 22
- [37] L. Collaboration, *LHCf experiment: Technical Design Report*. CERN. 22
- [38] J. Pinfold, *The MoEDAL experiment at the LHC*, EPJ Web Conf. **145** (2017) 12002. 22

- [39] A. Yamamoto, Y. Makida, R. Ruber, Y. Doi, T. Haruyama, F. Haug, H. ten Kate, M. Kawai, T. Kondo, Y. Kondo, J. Metselaar, S. Mizumaki, G. Olesen, O. Pavlov, S. Ravat, E. Sbrissa, K. Tanaka, T. Taylor, and H. Yamaoka, *The ATLAS central solenoid*, Nuclear Instruments and Methods in Physics Research Section A: Accelerators, Spectrometers, Detectors and Associated Equipment **584** no. 1, (2008) 53 – 74. <http://www.sciencedirect.com/science/article/pii/S0168900207020414>. 25
- [40] ATLAS Collaboration, *The ATLAS Inner Detector commissioning and calibration*, Eur. Phys. JC**70**, arXiv:1004.5293. 25
- [41] ATLAS Collaboration, *ATLAS Insertable B-Layer Technical Design Report*,. <https://cds.cern.ch/record/1291633>. 26, 39
- [42] G. A. et al., *ATLAS pixel detector electronics and sensors*, Journal of Instrumentation **3** no. 07, (2008) P07007. <http://stacks.iop.org/1748-0221/3/i=07/a=P07007>. 27
- [43] A. Bingül, *The ATLAS TRT and its Performance at LHC*, Journal of Physics: Conference Series **347** no. 1, (2012) 012025. <http://iopscience.iop.org/article/10.1088/1742-6596/347/1/012025/meta>. 27
- [44] T. A. Collaboration, *Studies of the performance of the ATLAS detector using cosmic-ray muons*, The European Physical Journal C **71** no. 3, (2011) 1593. <https://doi.org/10.1140/epjc/s10052-011-1593-6>. 28
- [45] ATLAS Collaboration, *ATLAS liquid-argon calorimeter: Technical Design Report*,. <https://cds.cern.ch/record/331061>. 30
- [46] ATLAS Collaboration, *ATLAS muon spectrometer: Technical design report*,. <https://cds.cern.ch/record/331068>. 31
- [47] ATLAS Collaboration, *Fast TracKer (FTK) Technical Design Report*,. <https://cds.cern.ch/record/1552953>. 32
- [48] A. Collaboration, *Performance of the ATLAS Trigger System in 2015*, Eur. Phys. J. **C77** (2017), arXiv:1611.09661 [hep-ex]. 35, 36, 39, 40, 41, 42, 43
- [49] E. Simoni, *The Topological Processor for the future ATLAS Level-1 Trigger: from design to commissioning*, arXiv:1406.4316. 36
- [50] ATLAS Collaboration, *The ATLAS Level-1 Calorimeter Trigger*, Journal of Instrumentation **3** no. 03, (2008) P03001. <http://stacks.iop.org/1748-0221/3/i=03/a=P03001>. 36

- [51] ATLAS Collaboration, *Performance of the ATLAS Trigger System in 2010*, Eur. Phys. J **C72** (2012), arXiv:1110.1530 [hep-ex]. 37, 38
- [52] ATLAS Collaboration, *Expected Performance of the ATLAS Experiment - Detector, Trigger and Physics*, arXiv:0901.0512 [hep-ex]. 37
- [53] ATLAS Collaboration, F. Miano, *The design and performance of the ATLAS Inner Detector trigger for Run 2 LHC collisions at $\sqrt{s} = 13$ TeV*, PoS **ICHEP2016** (2016) 856. 40
- [54] ATLAS Collaboration, *Performance of primary vertex reconstruction in proton-proton collisions at $\sqrt{s} = 7$ TeV in the ATLAS experiment*, Tech. Rep. ATLAS-CONF-2010-069, CERN, Geneva, Jul, 2010.
<http://cds.cern.ch/record/1281344>. 42
- [55] N. Ruthmann, Y. Nakahama, and C. Leonidopoulos, *Trigger Menu in 2016*, Tech. Rep. ATL-COM-DAQ-2016-137, CERN, Geneva, Sep, 2016.
<https://cds.cern.ch/record/2216366>. 44
- [56] ATLAS Collaboration, “Missing energy trigger public results.”
<https://twiki.cern.ch/twiki/bin/view/AtlasPublic/MissingEtTriggerPublicResults>. 45
- [57] ATLAS Collaboration, *ATLAS Computing : technical design report*,
<https://cds.cern.ch/record/837738>. 46
- [58] G. Barrand, et. al, *GAUDI - A software architecture and framework for building HEP data processing applications.*,
[http://dx.doi.org/10.1016/S0010-4655\(01\)00254-5](http://dx.doi.org/10.1016/S0010-4655(01)00254-5). 46
- [59] W. Lukas, *Fast Simulation for ATLAS: Atlassim-II and ISF*, J. Phys.: Conf. Ser **396** no. 022031, (2012). 47, 51
- [60] A. Buckley et al., *General-purpose event generators for LHC physics*, Phys. Rept. **504** (2011) 145–233, arXiv:1101.2599 [hep-ph]. 46
- [61] R. P. Feynman, *Very High-Energy Collisions of Hadrons*, Phys. Rev. Lett. **23** (1969) 1415–1417.
<https://link.aps.org/doi/10.1103/PhysRevLett.23.1415>. 47
- [62] T.-M. Yan and S. D. Drell, *The Parton Model and its Applications*, Int. J. Mod. Phys. **A29** (2014) 0071, arXiv:1409.0051 [hep-ph]. 47
- [63] J. D. Bjorken, *Asymptotic Sum Rules at Infinite Momentum*, Phys. Rev. **179** (1969) 1547–1553. <https://link.aps.org/doi/10.1103/PhysRev.179.1547>. 47

- [64] M. Dobbs and J. B. Hansen, *The HepMC C++ Monte Carlo event record for High Energy Physics*, Computer Physics Communications **134** no. 1, (2001) 41 – 46. <http://www.sciencedirect.com/science/article/pii/S0010465500001892>. 48
- [65] J. M. Campbell, J. Houston and W. Stirling, *Hard Interactions of Quarks and Gluons: A Primer of LHC Physics*, Rept. Prog. Phys. **70** no. 1, (2007). 49
- [66] V. N. Gribov and L. N. Lipatov, *Deep inelastic e p scattering in perturbation theory*, Sov. J. Nucl. Phys. **15** (1972) 438–450. [Yad. Fiz.15,781(1972)]. 49
- [67] G. Altarelli and G. Parisi, *Asymptotic Freedom in Parton Language*, Nucl. Phys. **B126** (1977) 298–318. 49
- [68] ZEUS, H1 Collaboration, F. D. Aaron et al., *Combined Measurement and QCD Analysis of the Inclusive e+ - p Scattering Cross Sections at HERA*, JHEP **01** (2010) 109, arXiv:0911.0884 [hep-ex]. 49
- [69] G. Corcella, et al., *HERWIG 6: an event generator of hadron emission reactions with interfering gluons (including supersymmetric processes)*, J. High Energy Phys. JHEP(**2001**) (2001). <http://iopscience.iop.org/article/10.1088/1126-6708/2001/01/010/meta>. 50
- [70] T.S., et al., *PYTHIA 6.4 physics and manual*, J. High Energy Phys. JHEP(**2006**) (2006). <http://iopscience.iop.org/article/10.1088/1126-6708/2006/05/026/meta>. 50
- [71] T. Gleisberg et al., *Event generation with SHERPA 1.1*, JHEP **02** (2009) 007. 50
- [72] Bernd A. Berg, *Introduction to Markov Chain Monte Carlo Simulations and their Statistical Analysis*, arXiv:cond-mat/0410490 [cond-mat]. 50
- [73] S. Catani, F. Krauss, R. Kuhn and B. Webber, *QCD Matrix Elements + Parton Showers*, JHEP **0111** (2001), arXiv:hep-ph/0109231 [hep-ph]. 50
- [74] M. L. Mangano, M. Moretti and R. Pittau, *Multijet Matrix Elements and Shower Evolution in Hadronic Collisions: $Wb\bar{b} + n$ Jets as a Case Study*, Nucl.Phys **B632** (2001), arXiv:0108069 [hep-ph]. 50
- [75] A. Kupco , *Cluster Hadronization in HERWIG 5.9*, arXiv:hep-ph/9906412 [hep-ph]. 50
- [76] B. Andersson, S. Mohanty and F. Soderberg, *Recent Developments in the Lund Model*, arXiv:hep-ph/0212122 [hep-ph]. 50
- [77] R. D. Field, *The Underlying Event in Hard Scattering Processes*, arXiv:hep-ph/0201192 [hep-ph]. 50

- [78] GEANT4 Collaboration, *Geant4 a simulation toolkit*, *Nucl. Instrum. Meth. A* **506** (2003). 51
- [79] *Vertex Reconstruction Performance of the ATLAS Detector at " $\sqrt{s} = 13 \text{ TeV}$ "*, Tech. Rep. ATL-PHYS-PUB-2015-026, CERN, Geneva, Jul, 2015.
<https://cds.cern.ch/record/2037717>. 52, 53
- [80] R. Fruhwirth, W. Waltenberger, and P. Vanlaer, *Adaptive vertex fitting*, *J. Phys. G* **34** (2007) N343. 52, 53
- [81] ATLAS Collaboration Collaboration, *Electron and photon energy calibration with the ATLAS detector using data collected in 2015 at $\sqrt{s} = 13 \text{ TeV}$* , Tech. Rep. ATL-PHYS-PUB-2016-015, CERN, Geneva, Aug, 2016.
<https://cds.cern.ch/record/2203514>. 53
- [82] ATLAS Collaboration, G. Aad et al., *Electron and photon energy calibration with the ATLAS detector using LHC Run 1 data*, *Eur. Phys. J.* **C74** no. 10, (2014) 3071, arXiv:1407.5063 [hep-ex]. 53
- [83] ATLAS Collaboration, T. A. collaboration, *Electron efficiency measurements with the ATLAS detector using the 2015 LHC proton-proton collision data*,. 54
- [84] ATLAS Collaboration, "Electron and photon performance public results."
<https://twiki.cern.ch/twiki/bin/view/AtlasPublic/ ElectronGammaPublicCollisionResults>. 54, 55
- [85] ATLAS Collaboration, M. Aaboud et al., *Measurement of the photon identification efficiencies with the ATLAS detector using LHC Run-1 data*, *Eur. Phys. J.* **C76** no. 12, (2016) 666, arXiv:1606.01813 [hep-ex]. 55
- [86] ATLAS Collaboration Collaboration, *Photon identification in 2015 ATLAS data*, Tech. Rep. ATL-PHYS-PUB-2016-014, CERN, Geneva, Aug, 2016.
<https://cds.cern.ch/record/2203125>. 55
- [87] ATLAS Collaboration, G. Aad et al., *Muon reconstruction performance of the ATLAS detector in proton–proton collision data at $\sqrt{s} = 13 \text{ TeV}$* , *Eur. Phys. J.* **C76** no. 5, (2016) 292, arXiv:1603.05598 [hep-ex]. 55, 57
- [88] ATLAS Collaboration, "Atlas muon combined performance with the full 2016 dataset." <https://atlas.web.cern.ch/Atlas/GROUPS/PHYSICS/PLOTS/MUON-2017-001/index.html>. 56
- [89] ATLAS Collaboration, *Electron reconstruction and identification efficiency measurements with the ATLAS detector using the 2011 LHC proton-proton collision data*, *Eur. Phys. J.* **74** no. 7, (2014), arXiv:1404.2240 [hep-ex]. 57

- [90] W. Lampl, et al., *Calorimeter Clustering Algorithms: Description and Performance*,
<https://cds.cern.ch/record/1099735>. 57
- [91] ATLAS Collaboration, G. Aad et al., *Topological cell clustering in the ATLAS calorimeters and its performance in LHC Run 1*, *Eur. Phys. J.* **C77** (2017) 490,
[arXiv:1603.02934 \[hep-ex\]](arXiv:1603.02934). 57
- [92] G. S. M. Cacciari, G. P. Salam, *The Anti- $k(t)$ jet clustering algorithm*, *JHEP* **0804** (2008), [arXiv:0802.1189 \[hep-ph\]](arXiv:0802.1189). 58
- [93] *Jet Calibration and Systematic Uncertainties for Jets Reconstructed in the ATLAS Detector at $\sqrt{s} = 13$ TeV*, Tech. Rep. ATL-PHYS-PUB-2015-015, CERN, Geneva, Jul, 2015. <https://cds.cern.ch/record/2037613>. 58
- [94] ATLAS Collaboration, T. A. collaboration, *Pile-up subtraction and suppression for jets in ATLAS*, 58
- [95] ATLAS Collaboration, T. A. collaboration, *Jet global sequential corrections with the ATLAS detector in proton-proton collisions at $\text{sqrt}(s) = 8$ TeV*, 58
- [96] *Data-driven determination of the energy scale and resolution of jets reconstructed in the ATLAS calorimeters using dijet and multijet events at $\sqrt{s} = 8$ TeV*, Tech. Rep. ATLAS-CONF-2015-017, CERN, Geneva, Apr, 2015.
<https://cds.cern.ch/record/2008678>. 58
- [97] *Tagging and suppression of pileup jets with the ATLAS detector*, Tech. Rep. ATLAS-CONF-2014-018, CERN, Geneva, May, 2014.
<https://cds.cern.ch/record/1700870>. 58
- [98] ATLAS Collaboration, M. Aaboud et al., *Identification and rejection of pile-up jets at high pseudorapidity with the ATLAS detector*, *Eur. Phys. J.* **C77** no. 9, (2017) 580,
[arXiv:1705.02211 \[hep-ex\]](arXiv:1705.02211). [Erratum: Eur. Phys. J.C77,no.10,712(2017)]. 58
- [99] ATLAS Collaboration, G. Aad et al., *Performance of b-Jet Identification in the ATLAS Experiment*, *JINST* **11** no. 04, (2016) P04008, [arXiv:1512.01094 \[hep-ex\]](arXiv:1512.01094). 58
- [100] N. Bartosik, *Diagram showing the common principle of identification of jets initiated by b-hadron decays*, 2016. http://bartosik.pp.ua/hep_sketches/btagging. 59